AIAA JOURNAL
Vol. 48, No. 9, September 2010

Large-Eddy Simulation of Jet Mixing in Supersonic Crossflows

Soshi Kawai* and Sanjiva K. Lele†
Stanford University, Stanford, California 94305

DOI: 10.2514/1.J050282

Large-eddy simulation of an underexpanded sonic jet injection into supersonic crossflows is performed to obtain insights into key physics of the jet mixing. A high-order compact differencing scheme with a recently developed localized artificial diffusivity scheme for discontinuity-capturing is used. Progressive mesh refinement study is conducted to quantify the broadband range of scales of turbulence that are resolved in the simulations. The simulations aim to reproduce the flow conditions reported in the experiments of Santiago and Dutton [Santiago, J. G., and Dutton, J. C., "Velocity Measurements of a Jet Injected into a Supersonic Crossflow," *Journal of Propulsion and Power*, Vol. 132, 1997, pp. 264–273] and elucidate the physics of the jet mixing. A detailed comparison with these data is shown. Statistics obtained by the large-eddy simulation with turbulent crossflow show good agreement with the experiment, and a series of mesh refinement studies shows reasonable grid convergence in the predicted mean and turbulent flow quantities. The present large-eddy simulation reproduces the large-scale dynamics of the flow and jet fluid entrainment into the boundary-layer separation regions upstream and downstream of the jet injection reported in previous experiments, but the richness of data provided by the large-eddy simulation allows a much deeper exploration of the flow physics. Key physics of the jet mixing in supersonic crossflows are highlighted by exploring the underlying unsteady phenomena. The effect of the approaching turbulent boundary layer on the jet mixing is investigated by comparing the results of jet injection into supersonic crossflows with turbulent and laminar crossflows.

I. Introduction

INSIDE a supersonic combustor, due to the limited flow residence time, the enhancement of supersonic turbulent mixing of jet fuel and crossflow air is a critical issue in developing supersonic airbreathing engines. Because of advances in computational power and numerical algorithms, the application of large-eddy simulation (LES) to compressible turbulent flows is the focus of significant research. The engineering motivation for compressible LES is to provide a more realistic turbulent flowfield than Reynolds-averaged Navier–Stokes (RANS) simulations and to elucidate the unsteady phenomena such as mixing, combustion, heat transfer, sound generation, unsteady loads, etc., which may be of interest to various practical applications. Jet mixing in a supersonic crossflow (JISC) is a good example of a flowfield in which compressible LES can play an important role in understanding the turbulent mixing mechanisms and help improve engineering prediction methods for high-speed turbulent flows.

Typical flow structures resulting from the injection of a sonic underexpanded transverse jet into a supersonic crossflow are illustrated in Fig. 1 [1,2]. The underexpanded jet expands through a Prandtl–Meyer fan at the lip of the jet orifice before the jet flow is compressed by the barrel shock and the Mach disk. The jet shear layer interacts with the shocks and breaks down to form a turbulent transverse jet that mixes with the crossflow stream. In a time-averaged sense, the jet forms a pair of counter-rotating vortices whose axis is aligned with the downstream direction. Because of the blockage of the supersonic crossflow by the jet, a bow shock is generated ahead of the jet. This causes boundary-layer separation upstream of injection and leads to the formation of a horseshoe vortex. Thus, the flowfield involves complex 3D unsteady shocks, contact surfaces, turbulence and their interactions. Accurately simulating these interactions is a significant challenge because the numerical algorithm needs to satisfy two competing requirements: the scheme needs to capture different types of discontinuities and also simultaneously resolve the broadband scales of turbulence.

Several experimental investigations have been conducted to understand the mechanisms of the jet mixing in a supersonic crossflow, which include detailed velocity measurements [3], time-averaged wall-pressure measurements [4] and temporally resolved flow visualizations and mixing characteristics with nonreactive [2,5] and combustible gaseous jets [1]. These measurements show the overall flow features and the dynamics of the jet shear layer and shocks along with extended flow data that can be used as validation data for numerical predictions. However, because of the difficulty in measuring the high-speed complex unsteady flowfields, experimental data are mainly obtained for certain transverse and longitudinal 2-D slices of the flowfield.

To obtain additional insights into the 3-D unsteady flow occurring in the supersonic jet mixing, numerical simulation is an attractive choice. Investigations of detailed time-averaged flowfields have been carried out using RANS simulation [6]. However, RANS simulation does not resolve the unsteady turbulent eddy structures responsible for turbulent mixing, thus being unable to elucidate the unsteady physics of the jet mixing. LES [7] and detached-eddy simulation (DES) [8] have been performed and have showed the presence of some large-scale structures. However, these large-scale structures are somewhat obscure, and fine turbulent eddy structures are missing in these simulations. This is primarily because in these calculations the conventional low-order upwind-biased finite volume schemes were employed to discretize the governing equations with limited grid resolution. These schemes work well in the sense of discontinuity-capturing for the bow shock, barrel shock, Mach disk, and jet contact surface (which are all observed in an underexpanded sonic jet in a supersonic crossflow), but are too dissipative for use in LES to properly resolve the broadband scales of turbulence. Although there are high-order upwind-biased schemes [e.g., essentially non-oscillatory (WENO) schemes by Jiang and Shu [9]], [10,11] showed that the numerical dissipation introduced by the high-order WENO scheme overwhelms a large range of scales, although the order of accuracy of these schemes can be very high. The result illustrates that the upwind-biased schemes (even if the formal order of accuracy is high) are often too dissipative for use in LES to properly resolve the turbulent eddy structures using limited computational resources. It is essential for LES to properly resolve the energy-containing scales of

---

Presented as Paper 2009-3795 at the 19th AIAA Computational Fluid Dynamics Conference, San Antonio, TX, 22–25 June 2009; received 8 October 2009; revision received 14 January 2010; accepted for publication 3 February 2010.

*Postdoctoral Fellow, Center for Turbulence Research. Senior Member AIAA.

†Professor, Department of Aeronautics and Astronautics and Department of Mechanical Engineering. Member AIAA.

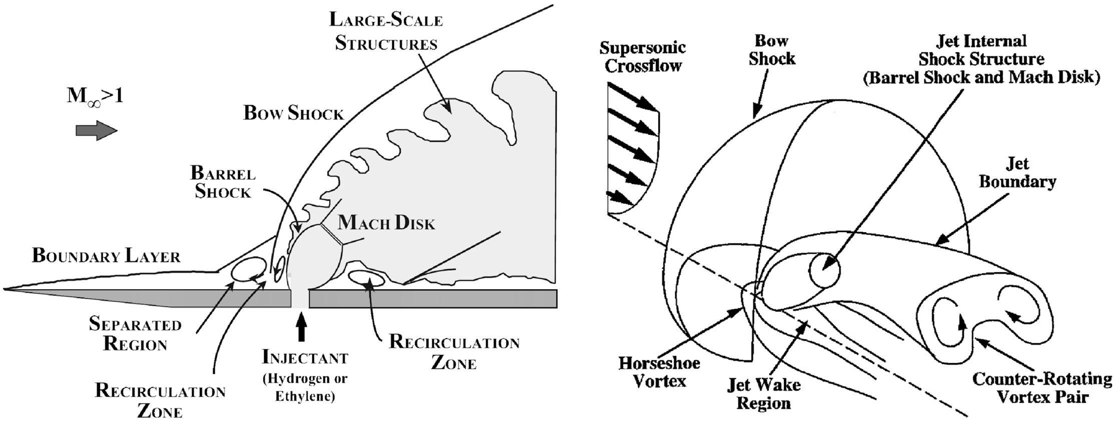

a) Instantaneous side-view at symmetry plane (from Ben-Yakar et al. [1])

b) Time-averaged 3-D perspective-view (from Gruber et al. [2])

Fig. 1 Schematics of the transverse injection of an underexpanded jet into a supersonic crossflow.

turbulence and avoid damping the turbulence artificially. Therefore, LES of the supersonic jet mixing presents challenges for simultaneously capturing complex unsteady shocks and contact surfaces and resolving the broadband turbulent eddying motions present in high Reynolds number flows. It should also be noted that DES-type approaches including hybrid RANS/LES methods in which near wall turbulence is simulated with RANS are unable to account for the effect of the turbulent eddies in the crossflow boundary layer on the jet mixing. The present study explores the effect of the turbulent crossflow and it turns out that the turbulent structures in the crossflow boundary layer are an important factor in determining the behavior of jet fluid stirring and subsequent mixing (also presumably resultant ignition).

The main objective of this paper is to understand the key physics of the jet mixing in supersonic crossflows underlying the observed unsteady phenomena. Emphasis in this paper is placed on 1) detailed validation and a progressive mesh refinement study to assess the quality of the simulated results, 2) identifying the key vortex structures and large-scale dynamics in the flow that are responsible for the jet mixing, and 3) understanding the effect of the approaching turbulent boundary layer on the jet mixing. LES of an underexpanded sonic jet injection into supersonic crossflows is performed to obtain insights into the physics of the jet mixing. To properly resolve the turbulence while capturing the discontinuities, we use a high-order nondissipative compact differencing scheme [12] coupled with recently developed localized artificial diffusivity (LAD) methodology [13]. The high-resolution characteristics of the compact scheme enable us to resolve turbulence, whereas the LAD method is used to capture the unsteady shocks and contact surfaces. A progressive mesh refinement study is performed to quantify the broadband range of scales of turbulence that are resolved in the simulations. The mesh refinement in combination with the high-resolution nondissipative numerical scheme allows for proper resolution of the turbulence. The flow conditions are set based on the experiment of Santiago and Dutton [3], Everett et al. [4], and VanLerberghe et al. [5], where the crossflow Mach number $M_\infty = 1.6$, the Reynolds number based on the crossflow conditions and the diameter of the nozzle exit $Re_D = 2.4 \times 10^4$, and the jet-to-crossflow momentum flux ratio $J = 1.7$. The numerical results are compared with the experimental data.

As a prelude to the discussions of JISC, the statistics of the $M_\infty = 1.6$ supersonic turbulent boundary layer are shown in Sec. III.A. The turbulent boundary layer is used for the JISC with turbulent crossflow. In Sec. III.B simulated time-averaged flowfields are presented, which illustrates the overall flow structures. Detailed comparisons between the LES and available experiment data and the results of a series of mesh refinement studies are given in Sec. III.C. Key physics of the jet mixing in a supersonic crossflow are highlighted by exploring the flow physics underlying the observed unsteady phenomena in Sec. III.D. Section III.E illustrates the effect of approaching turbulent boundary layer on the jet mixing by comparing the results of JISC with turbulent and laminar crossflows.

II. Mathematical Models

A. Governing Equations

The compressible Navier–Stokes equations for an ideal nonreactive gas are

$$\frac{\partial \rho}{\partial t} + \nabla \cdot (\rho \boldsymbol{u}) = 0 \tag{1}$$

$$\frac{\partial \rho \boldsymbol{u}}{\partial t} + \nabla \cdot (\rho \boldsymbol{u}\boldsymbol{u} + p\underline{\boldsymbol{\delta}} - \underline{\boldsymbol{\tau}}) = 0 \tag{2}$$

$$\frac{\partial E}{\partial t} + \nabla \cdot [E\boldsymbol{u} + (p\underline{\boldsymbol{\delta}} - \underline{\boldsymbol{\tau}}) \cdot \boldsymbol{u} - \kappa \nabla T] = 0 \tag{3}$$

$$\frac{\partial \rho Y_i}{\partial t} + \nabla \cdot (\rho \boldsymbol{u} Y_i) - \nabla(\rho D_i \nabla Y_i) = 0 \tag{4}$$

where ρ is the density, $\boldsymbol{u}$ is the velocity vector, p is the static pressure defined by $p = \rho R T$, E is the total energy defined by

$$E = \frac{p}{\gamma - 1} + \frac{1}{2}\rho \boldsymbol{u} \cdot \boldsymbol{u}$$

T is the temperature, γ (1.4) is the ratio of specific heats, R is the gas constant, κ is the thermal conductivity, and $\underline{\boldsymbol{\delta}}$ is the unit tensor. In addition to the Navier–Stokes equations, the transport Eq. (4) for a passive scalar of jet fluid is solved to investigate the mixing between the jet fluid and crossflow, where D_i is the diffusion coefficient for the passive scalar. The viscous stress tensor $\underline{\boldsymbol{\tau}}$ (for a Newtonian fluid) is

$$\underline{\boldsymbol{\tau}} = \mu(2\underline{\boldsymbol{S}}) + \left(\beta - \frac{2}{3}\mu\right)(\nabla \cdot \boldsymbol{u})\underline{\boldsymbol{\delta}} \tag{5}$$

where μ is the dynamic (shear) viscosity, β is the bulk viscosity, $\underline{\boldsymbol{S}}$ is the strain rate tensor, and $\underline{\boldsymbol{S}} = \frac{1}{2}(\nabla \boldsymbol{u} + (\nabla \boldsymbol{u})^T)$. The dynamic viscosity in the fluid μ_f is computed by Sutherland's law and the bulk viscosity β_f is set to 0. The thermal conductivity κ_f is computed by $\kappa_f = \mu_f C_p / Pr$, where C_p is the specific heat constant and the Prandtl number $Pr = 0.72$. The passive scalar diffusion coefficient $D_{f,i}$ is computed by $D_{f,i} = \mu_f / \rho Sc$, where Sc is the Schmidt number and is on the order of unity. The f subscripts denote fluid transport coefficients in Eq. (6).

In the compressible LES, the Navier–Stokes equations are spatially filtered, which introduces Favre-averaged variables. Spatially filtered Navier–Stokes equations are similar to the

Navier–Stokes equations but include additional subgrid-scale stress, heat flux, and species diffusion terms that need to be modeled.

B. Numerical Schemes

The spatially filtered Navier–Stokes equations in the conservative form are solved in generalized curvilinear coordinates, where spatial derivatives are evaluated by a sixth-order compact differencing scheme [12]. Because of their spectral-like resolution and nondissipative characteristics, high-order compact differencing schemes are an attractive choice for LES to properly resolve the broadband scales of turbulence.

When central differencing schemes, such as high-order compact differencing schemes, are applied to solve flows that involve steep gradients (e.g., due to shock waves, contact surfaces, or material discontinuities), nonphysical spurious oscillations that make the simulation unstable are generated. The localized artificial diffusivity (LAD) method [13] is used to capture the discontinuities in the flow. The method is based on adding grid-dependent artificial fluid transport coefficients to the physical transport coefficients appearing in Eqs. (3–5) proposed by Cook [14]:

$$\begin{aligned} \mu &= \mu_f + \mu^*, \qquad & \beta &= \beta_f + \beta^* \\ \kappa &= \kappa_f + \kappa^*, \qquad & D_i &= D_{f,i} + D_i^* \end{aligned} \tag{6}$$

where the f subscripts and asterisks denote fluid and artificial transport coefficients. According to [14] the artificial fluid properties μ^*, β^*, κ^*, and D_i^* serve as a multipurpose model for the subgrid-scale transport, for shock-capturing, contact-surface capturing, and material-interface capturing.

We model the artificial fluid transport coefficients to automatically vanish in smooth well-resolved regions and locally provide damping in nonsmooth regions to capture different types of discontinuities. Thus, the method does not affect smooth well-resolved flow regions, and the high-resolution characteristics of a high-order compact scheme are preserved in smooth regions while retaining the discontinuity-capturing capability. The localized artificial diffusivity on a multidimensional generalized coordinate system is modeled as [13]

$$\mu^* = C_\mu \rho \overline{\left| \sum_{l=1}^{3} \frac{\partial^4 S}{\partial \xi_l^4} \Delta \xi_l^4 \Delta_{l,\mu}^2 \right|} \tag{7}$$

$$\begin{aligned} \beta^* &= C_\beta \rho f_{sw} \overline{\left| \sum_{l=1}^{3} \frac{\partial^4 \nabla\cdot\boldsymbol{u}}{\partial \xi_l^4} \Delta \xi_l^4 \Delta_{l,\beta}^2 \right|} \\ f_{sw} &= \frac{H(-\nabla\cdot\boldsymbol{u})(\nabla\cdot\boldsymbol{u})^2}{(\nabla\cdot\boldsymbol{u})^2 + (\nabla\times\boldsymbol{u})^2 + \varepsilon} \end{aligned} \tag{8}$$

$$\kappa^* = C_\kappa \frac{\rho c_s}{T} \overline{\left| \sum_{l=1}^{3} \frac{\partial^4 e}{\partial \xi_l^4} \Delta \xi_l^4 \Delta_{l,\kappa} \right|} \tag{9}$$

$$\begin{aligned} D_i^* &= C_D c_s \overline{\left| \sum_{l=1}^{3} \frac{\partial^4 Y_i}{\partial \xi_l^4} \Delta \xi_l^4 \Delta_{l,D_i} \right|} \\ &\quad + C_Y \overline{c_s [Y_i - 1] H(Y_i - 1) - Y_i [1 - H(Y_i)] \Delta_{Y_i}} \end{aligned} \tag{10}$$

The method is the extension of the original artificial diffusivity scheme proposed by Cook [14], curvilinear mesh extension of Kawai and Lele [15], and dilatation-based bulk viscosity with the length-scaling modification of Mani et al. [16]. C_μ, C_β, C_κ, C_D, and C_Y are dimensionless user-specified constants; S is the magnitude of the strain rate tensor; e is the internal energy defined by

$$e = \frac{1}{\gamma - 1} \frac{p}{\rho}$$

c_s is the speed of sound; H is the Heaviside function; ξ_l refers to generalized coordinates ξ, η, and ζ when l is 1, 2, and 3, respectively; and $\varepsilon = 10^{-32}$ is a small positive constant to prevent division by zero in the region where both $\nabla\cdot\boldsymbol{u}$ and $\nabla\times\boldsymbol{u}$ are zero. The overbar denotes an approximate truncated-Gaussian filter [17]. The $\Delta\xi_l$ and $\Delta_{l,\bullet}$ are the grid spacing in the computational space and physical space; $\Delta\xi_l$ is usually set to 1. We define the grid spacing $\Delta_{l,\bullet}$ as follows:

$$\begin{aligned} \Delta_{l,\mu} &= |\boldsymbol{\Delta x}_l|, \qquad & \Delta_{l,\beta} &= \left| \boldsymbol{\Delta x}_l \cdot \frac{\nabla\boldsymbol{\rho}}{|\nabla\boldsymbol{\rho}|} \right| \\ \Delta_{l,\kappa} &= \left| \boldsymbol{\Delta x}_l \cdot \frac{\nabla\boldsymbol{e}}{|\nabla\boldsymbol{e}|} \right|, \qquad & \Delta_{l,D_i} &= \left| \boldsymbol{\Delta x}_l \cdot \frac{\nabla\boldsymbol{Y}_i}{|\nabla\boldsymbol{Y}_i|} \right| \end{aligned} \tag{11}$$

The $\boldsymbol{\Delta x}_l$ is the local displacement vector along the grid line in the ξ_l direction and is defined as

$$\boldsymbol{\Delta\, x}_l = \left(\frac{x_{i+1} - x_{i-1}}{2}, \frac{y_{i+1} - y_{i-1}}{2}, \frac{z_{i+1} - z_{i-1}}{2}\right)^T$$

Thus, $\Delta_{l,\beta}$, $\Delta_{l,\kappa}$, and Δ_{l,D_i} are the grid spacing in the ξ_l direction perpendicular to the shock waves, contact surfaces, and material discontinuities. The length scalings used here are the natural extension based on [16]. Δ_{Y_i} in Eq. (10) is the grid spacing in the physical space defined by

$$\Delta_{Y_i} = \frac{\sum_{l=1}^{3} \left| \frac{\partial^4 Y_i}{\partial \xi_l^4} \right| \Delta_{l,D_i}}{\sqrt{\sum_{l=1}^{3} \left(\frac{\partial^4 Yi}{\partial \xi_l^4} \right)^2} + \varepsilon}$$

The fourth-derivative terms in Eqs. (7–10) are evaluated by using a fourth-order explicit scheme [15]. The dimensionless user-specified constants in Eqs. (7–10) are set to $C_\mu = 0.002$, $C_\beta = 1.75$, $C_\kappa = 0.01$, $C_D = 0.01$, and $C_Y = 100$ in this study based on our previous investigations [13,15]. These constants allows the scheme to capture discontinuities and not to introduce excessive dissipation. A van Driest wall damping function multiplies the grid spacing ($\Delta_{l,\mu}$ and $\Delta_{l,\beta}$) in the LAD method to force the artificial viscosity to vanish in the near wall portion of the boundary layers. The present numerical approach shows superior performance in simulating flows that involve shocks, turbulence, and their interactions compared with high-order upwind-biased schemes. The further detailed analysis of the performance of the LAD method for LES of compressible turbulent flows may be found in [13].

An eighth-order low-pass spatial filtering scheme [12,18] with $\alpha_f = 0.495$ is applied to the conservative variables once in each direction after every three time steps to ensure numerical stability. The fully implicit scheme [19,20] that is derived by combining alternative-direction implicit factorization [21] with the lower–upper symmetric Gauss–Seidel method [22] is used for time integration. The implicit portion of the algorithm uses second-order-accurate three-point backward differencing for the derivative. Three steps of subiterations (Newton–Raphson iteration) are adopted to minimize the errors due to the linearization in the implicit scheme. In the present study, the nondimensional computational time step is fixed to $\Delta t U_\infty / D = 9.6 \times 10^{-4}$ at which the maximum inviscid Courant–Friedrichs–Lewy number is less than 1.0, where D is the diameter of the nozzle exit. The present time-integration scheme with this time-step size should be sufficiently accurate, based on our previous study [13].

C. Flow Conditions and Computational Grids

To validate the present LES of JISC, the flow condition examined in this study is based on the experiments of Santiago and Dutton [3], Everett et al. [4], and VanLerberghe et al. [5]. The computation uses a freestream Mach number of $M_\infty = 1.6$ and a Reynolds number based on the freestream conditions and the diameter of the nozzle exit:

$$Re_D = \frac{\rho_\infty U_\infty D}{\mu_\infty} = 2.4 \times 10^4$$

The density and pressure ratio between the nozzle chamber and crossflow are $\rho_{0j}/\rho_\infty = 5.55$ and $p_{oj}/p_\infty = 8.40$. Based on these flow conditions, the resulting jet-to-crossflow momentum flux ratio is $J = \rho_j u_j^2/\rho_\infty u_\infty^2 = 1.7$. We use same fluid (air) for both the jet and crossflow fluids based on the experiments. Only the Reynolds number Re_D differs from the experiment; a Reynolds number approximately six times lower than the Re_D in the experiments is chosen to maintain the LES resolution requirement under currently acceptable computational costs. Although the Reynolds number is not matched, the upstream boundary-layer thickness is matched with the experiment at $x/D = -5$, where $\delta_{99} = 0.775D$ (3.1 mm).

To investigate the effect of the approaching turbulent boundary layer on the mixing mechanisms, LES of JISC with both the cases of an incoming laminar and turbulent boundary layer are considered in this study. The results of a turbulent-crossflow boundary layer are compared with those from the laminar crossflow case. Note that the experimental measurement of the mean velocity profile of the approaching boundary layer shows a turbulent-boundary-layer profile [3]. Figure 2 shows the schematic of the simulation of the JISC with a turbulent boundary layer. We conduct concurrent simulations of a supersonic turbulent boundary layer (STBL) that are coupled with the JISC computation. The inflow conditions for the LES of JISC with STBL are extracted from the plane of concurrent LES of STBL, where $\delta_{99} = 0.775D$. In the concurrent LES of STBL, the Reynolds number is matched with the JISC simulation, $Re_D = 2.4 \times 10^4$. The corresponding Reynolds number based on the boundary-layer thickness at the extracted plane is $Re_{\delta 99} = 18600$, where $\delta_{99} = 0.775D$ (3.1 mm). The rescaling-reintroducing method [23] is used to generate the inflow conditions for the LES of STBL, as shown in Fig. 2. The flow quantities at the $8D$ downstream location are rescaled and reintroduced for the inflow conditions. Instantaneous density gradient magnitude contours at the midline plane $z/D = 0$ and streamwise velocity contours at the wall-parallel plane close to the wall ($y^+ = 18.5$) are shown in Fig. 2. Typical low-speed streaks (light gray-colored regions) in the STBL and instantaneous reverse-flow regions (light colored regions) in the JISC are clearly observed in the wall-parallel plane. For the JISC with incoming laminar boundary-layer case, mean physical properties at the crossflow inlet boundary at $x/D = -5$ on the background mesh are adopted from the profiles obtained by a two-dimensional laminar boundary-layer simulation.

Figure 3 shows the grid geometry of the computational domain (without showing the STBL mesh) employed in the present study. Every fifth grid point on the fine mesh is presented in the figure. Overset grids consist of three structured grids: background, nozzle, and nozzle-axis grids. The nozzle grid employs a cylindrical polar topology. To preclude the appearance of a pole in this structure, the nozzle grid does not include the region where the radius approaches zero. The nozzle-axis grid covers the region of small radius in the cylindrical polar within the nozzle grid. The geometry of the nozzle matches the experiment [3–5]. The computational test section of the background mesh extends from the center of the nozzle exit to $5D$ upstream and downstream in the streamwise direction ($-5 \leq x/D \leq 5$), $3.3D$ in the wall-normal direction ($0 \leq y/D \leq 3.3$) and $2D$ on both sides in the spanwise direction ($-2 \leq z/D \leq 2$). In the focused region, a uniformly spaced grid is adopted in the streamwise and spanwise directions. In the wall-normal direction, the grid is clustered near the wall in the region $y/D = 0$ to 0.3 and then a uniformly spaced grid is used for $y/D = 0.3$ to 3.3. We introduce large buffer layers with lengths of $20D$, $10D$ and $10D$ at the outlet, on both the side and the upper boundaries. The grid is smoothly stretched (the grid stretching factor is smoothly increased) in the buffer layers toward the boundaries, thus coarsening the mesh toward the boundaries. The maximum grid stretching factor is approximately 1.15 in each direction. The large buffer layers with coarsened mesh damp turbulent fluctuations and avoid spurious reflection from the boundaries. The computational test section for the STBL mesh extends $10D$, $4D$ and $1.6D$ in the streamwise, spanwise, and wall-normal directions. Similar to the background mesh for JISC, buffer layers with lengths of $10D$ and $10D$ are placed at the spanwise and

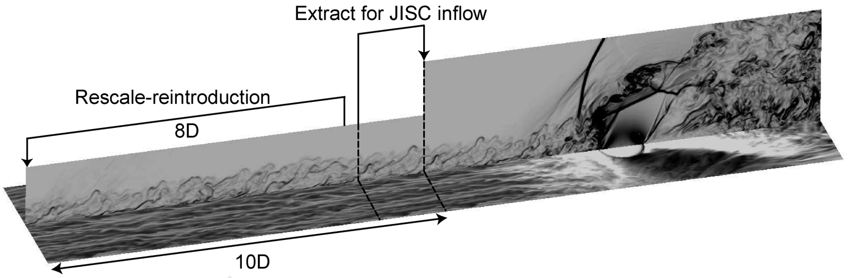

Fig. 2 JISC with incoming supersonic turbulent boundary layer. Density gradient magnitude contours at midline plane $z/D = 0$ and streamwise velocity contours at wall-parallel plane close to the wall ($y^+ = 18.5$) on fine mesh.

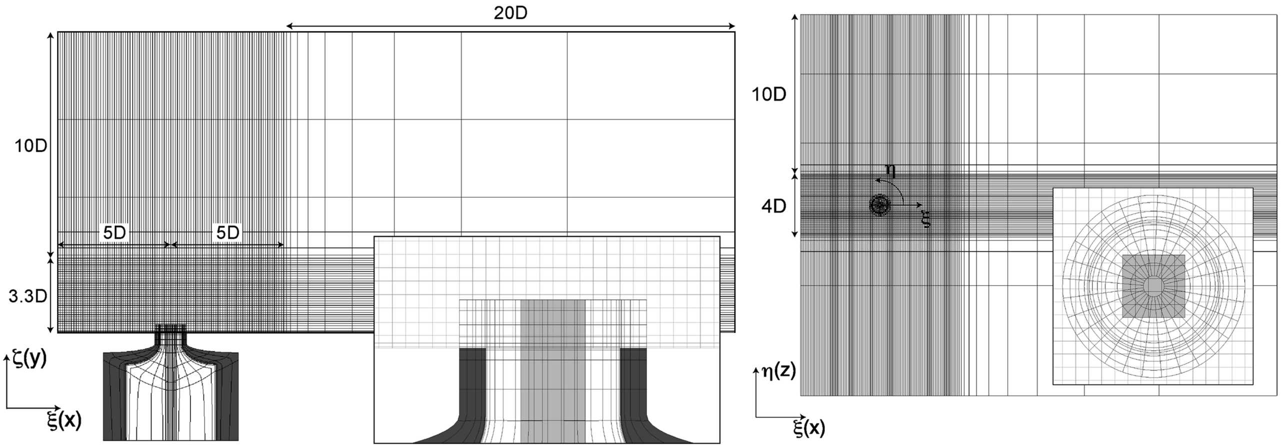

Fig. 3 Computational grids: background, nozzle, and nozzle-axis grids (every fifth grid point on fine mesh). Side view at symmetry plane $z/D = 0$ on left and top view on right. Inside wall regions as a part of the nozzle grid in dark gray-colored surfaces and nozzle-axis grid in light gray-colored surfaces.

Table 1 Computational grids for JISC background mesh and STBL mesh

Grid	N_ξ	N_η	N_ζ	Total (million)	Δ^+ in ξ	Δ^+ in η	Δ^+ in ζ
				JISC background mesh			
Fine	551	243	204	27.3	14.5	14.5	1–14.5
Medium	411	187	154	11.8	20.5	20.5	1–20.5
Coarse	301	131	115	4.5	29.0	29.0	1–29.0
				STBL mesh			
Fine	361	243	120	10.5	20.5	14.5	1–14.5
Medium	361	187	101	6.8	20.5	20.5	1–20.5
Coarse	251	131	87	2.9	29.0	29.0	1–29.0

the upper boundaries. The grid distribution is the same as that of the background mesh. Communication between the grids for the overset meshes is handled through a two-point fringe at boundaries by using a fourth-order Lagrangian interpolation [24]. The bottom boundary of the nozzle is set to nozzle chamber conditions based on the experiments ($\rho_{0j}/\rho_\infty = 5.55$, $p_{oj}/p_\infty = 8.40$ and $\boldsymbol{u} = 0$, the resulting $J = 1.7$). The solid wall boundary condition is treated as a nonslip adiabatic wall.

Three levels of mesh refinement by the factor of $\sqrt{2}$ in each direction are conducted on the background mesh and the mesh for simulating the STBL for the turbulent crossflow. Table 1 summarizes the number of grid points and the grid resolution. The grid resolutions in wall units are based on the wall friction coefficient at $x/D = -5$ measured in the experiment [3] and for the reduced Reynolds number used in this study. The number of grid points for the nozzle mesh and nozzle-axis mesh are $54 \times 149 \times 75$ and $25 \times 25 \times 75$ in the ξ, η, and ζ directions, respectively. The grid resolutions for the nozzle and nozzle-axis meshes are designed based on the fine background mesh. The total number of grid points for the JISC with STBL on the fine mesh is 38.5 million points. The fine mesh calculation was performed on Japan Aerospace Exploration Agency (JAXA) Supercomputer System (quad-core CPU with a clock rate of 2.5 GHz) at JAXA, which requires approximately 90,000 core hours to collect the flow data over 100 time units tU_∞/D.

III. Results

Statistical data discussed in the following are based on averaging flowfields over 100 time units tU_∞/D. In this time scale, the freestream flow passes through a distance of $100D$.

A. Statistics of Turbulent Boundary Layer

The computed statistics of the $M_\infty = 1.6$ supersonic turbulent boundary layer for the inflow conditions of JISC with STBL simulations are addressed here. The three levels of mesh refinement are summarized in Table 1.

The mean streamwise velocity profile in a semilogarithmic plot using the van Driest transformation [25],

$$U^+_{\mathrm{VD}} = \int_0^{U^+} \left(\frac{\rho}{\rho_w}\right)^{1/2} \mathrm{d}U^+ \tag{12}$$

and the variances of three velocity components are plotted in Fig. 4. The statistics are averaged in time and in the spanwise direction and are denoted as $\langle\langle\,\rangle\rangle$. The direct numerical simulation (DNS) data for the Mach 2 supersonic turbulent boundary at $Re_\delta = 17400$ by Pirozzoli et al. [26], and the expected linear scaling in the viscous sublayer $U^+_{\mathrm{VD}} = y^+$, and the logarithmic scaling $U^+_{\mathrm{VD}} = \frac{1}{k}\log(y^+) + C$ are also included in the figure for comparison (there are no available experimental or DNS data at the precise flow conditions examined in this paper). The von Kármán constant is set to $k = 0.41$, and the log law constant is set to $C = 5.2$, as found in the previous DNS [26,27]. The mean and variances of velocity on the fine and medium meshes show good grid convergence and excellent agreement with the DNS data with a fully developed turbulent-boundary-layer profile with a logarithmic region appearing clearly in the range of $30 < y^+ < 150$. The coarse mesh shows a shift in the logarithmic region and overpredicts the peak variances of streamwise velocity.

B. Time-Averaged Flowfields

Figure 5a shows time-averaged Mach number distributions with streamlines at midline, wall-normal, and cross-view planes. The Mach number contours clearly show the shock structures, such as the front bow shock, barrel shock, Mach disk, reflected shock from the triple line (the intersection of the barrel shock and Mach disk), and separation shock at the front of bow shock. The upstream separation shock is not as strong as the other shocks, the contours slightly change from the dark gray to light gray (from preshock to postshock) and interact with the bow shock. The streamlines show that most of the jet fluid passes through the barrel shock and Mach disk and then turns downstream. Upstream of the jet, a recirculation region is observed. The recirculation forms a horseshoe separation

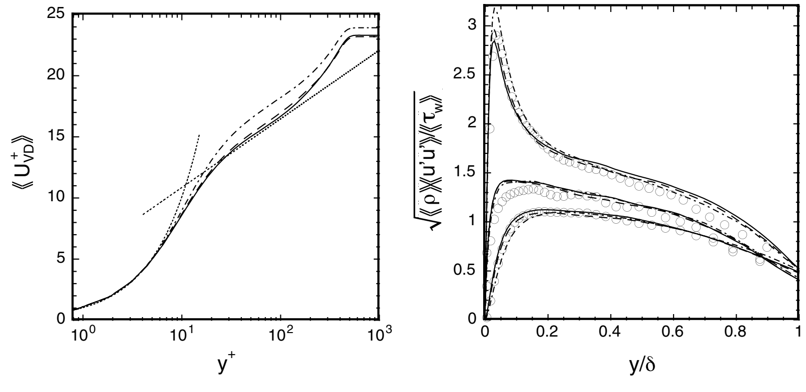

a) Mean streamwise velocity

b) Variance of velocity: upper curves, streamwise; middle curves, spanwise; lower curves, wall-normal

Fig. 4 Mean and variances of velocity profiles in $M_\infty = 1.6$ supersonic turbulent boundary layer. Solid line: fine mesh; dashed line: medium mesh; dashed-dotted line: coarse mesh; dotted lines: $U^+_{\mathrm{VD}} = y^+$ and $U^+_{\mathrm{VD}} = 1/0.41\log(y^+) + 5.2$; ○: DNS by Pirozzoli et al. [26].

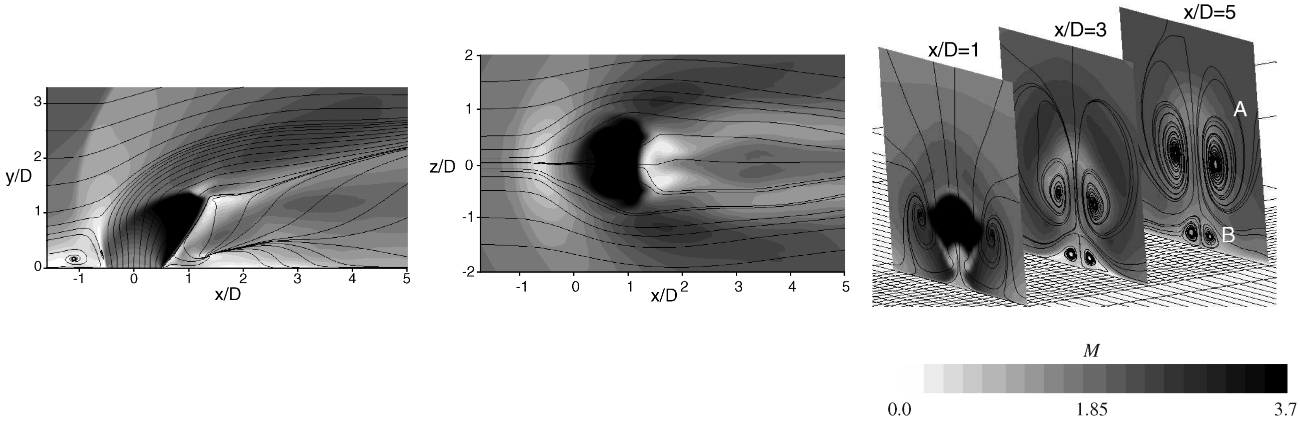

a) Mach number with streamlines

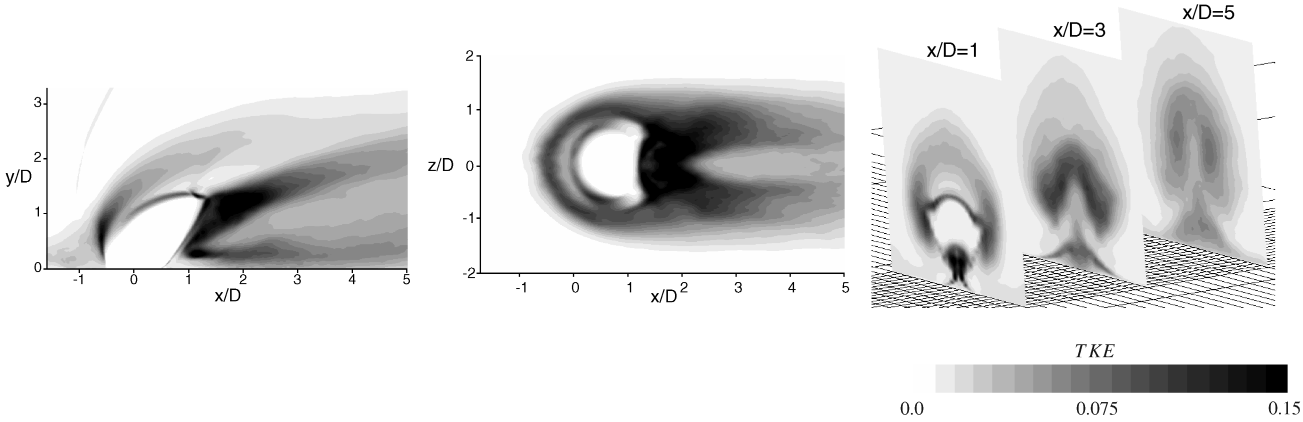

b) Turbulent kinetic energy

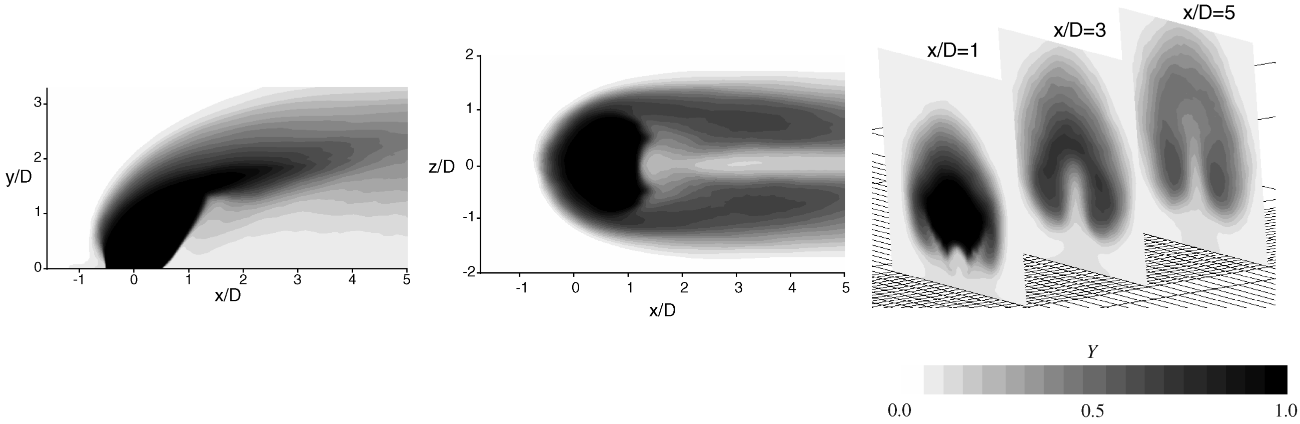

c) Jet fluid (passive scalar Y)

Fig. 5 Time-averaged Mach number distributions with streamlines, turbulent kinetic energy, and time-averaged jet fluid (passive scalar Y) distributions obtained by LES of JISC with STBL simulation on fine mesh: side view at midline plane $z/D = 0$ on the left, top view at wall-parallel plane $y/D = 1$ in the middle and cross-view planes of $x/D = 1$, 3, and 5 on the right. 20 equally spaced contours.

vortex ahead of the foot of the bow shock. The horseshoe vortex curves sideways from the midline plane $z/D = 0$. The top view shows that the streamlines diverge laterally after the crossflow deflects through the bow shock and then converge downstream, due to the low pressure downstream of the jet. Two pairs of counter-rotating vortices are clearly visible downstream of the jet injection in the cross view of the time-averaged flowfield; one is the counter-rotating jet vortices (A in Fig. 5a) as often discussed in the literature [2,3,6], and the other is the pair of boundary-layer separation vortices (B in Fig. 5a) along the symmetric plane induced by the suction of the counter-rotating jet vortices.

Time-averaged turbulent kinetic energy (TKE), $(\langle u'u'\rangle + \langle v'v'\rangle + \langle w'w'\rangle)/2U_\infty^2$, and jet fluid (passive scalar Y) distributions are shown in Figs. 5b and 5c. Three high-TKE regions are identified at the windward and leeward boundaries of the jet and under the leeward jet boundary in the side view. The first two high-TKE regions surround the jet boundary. As shown in the cross view in Fig. 5b, the high TKE under the leeward jet boundary observed in the side view originates from the boundary-layer separation under the counter-rotating jet vortices along the symmetric plane. These high-intensity regions in the TKE correspond to the regions where strong vortex structures are observed in the instantaneous flowfield, as will be discussed in Sec. III.D. Time-averaged jet fluid distributions in Fig. 5c show that the jet fluid is progressively diluted in the regions where high TKE is observed, suggesting that the turbulent eddies are responsible for the turbulent stirring and subsequent mixing. The cross view shows the jet fluid entrainment into the boundary-layer separation vortices downstream of the jet.

C. Statistics

Although very limited detailed quantitative data are available in the literature for this complex high-speed flow, fortunately, Santiago and Dutton [3] and Everett et al. [4] provide extensive flow data for the condition examined in this study. First, it is necessary to mention the uncertainty associated with the experimental data to properly use it to validate the LES data. The experimental data have a certain level of experimental noise and limited resolution as evidenced in the time-averaged and variance of velocity distributions shown in Fig. 6c (also will be shown in Figs. 9 and 12c). Also, two separate experimental measurements show some degree of differences, and the experimental data show asymmetry across the $z = 0$ plane. It should also be noted that the present LES employs a Reynolds number approximately 6 times lower than that of the experiment to maintain the high-LES-resolution requirement under currently acceptable computational costs. For these reasons, precise quantitative agreement between the present LES and the experiment cannot be expected. Nevertheless, comparisons to experimental data allow us to establish a certain level of confidence in the simulations. In addition to the comparison, we conduct a series of progressive mesh refinement studies to quantify the range of scales of turbulence that are resolved in the simulations.

1. Time-Averaged Velocities

Comparisons of the mean streamwise and wall-normal velocity distributions between the LES with turbulent and laminar crossflows and the experiment [3] at the midline plane $z/D = 0$ are shown in Fig. 6. The results obtained for the fine mesh are shown here. Figures 7 and 8 quantitatively compare the mean velocity distributions obtained for the three levels of mesh resolution and the experimental data at upstream and downstream stations $x/D = -1.5$, 2, 3, 4, and 5. The mesh refinement study shows that the time-averaged flow quantities are grid converged. Significant discrepancy between the LES and experiment is observed close to the wall in the region immediately downstream of the jet, where the LES shows a recirculation region, whereas the experimental data do not indicate this (Fig. 6). The reason for this discrepancy is not clear, but overall the locations of the shock structures and downstream jet development agree reasonably well with the experiment.

Better agreement with the experiment is obtained for the LES results using the turbulent crossflow. Differences between the turbulent and laminar crossflow are especially noticeable in the upstream and downstream separating regions. The turbulent crossflow delays the boundary-layer separation upstream of the jet, and smaller upstream and downstream recirculation regions are obtained compared with the laminar crossflow. The resultant separation shock occurring ahead of the bow shock is also better predicted with the turbulent crossflow. Note the dramatic improvement in the predicted mean streamwise and wall-normal velocity profiles at the $x/D = -1.5$ station for the turbulent-crossflow calculation, as shown in Figs. 6, 7a, and 8a. In the laminar case, the upstream separation region extends to the upstream inlet boundary, thus not showing the separation shock in the domain shown in Fig. 6.

In the downstream jet development, the predicted mean velocity is relatively less sensitive to the crossflow conditions. Both the laminar and turbulent crossflows show very similar jet development. The mean streamwise velocity profiles predicted by the LES are in good agreement with the experiment with the possible exception of the strength of the streamwise flow in the separated flow region immediately downstream of jet injection and downstream of the separated region. Regarding the wall-normal velocity profiles downstream of the jet injection, the LES overpredicts the upwash at location $x/D = 2$. The wall-normal velocity distributions at $x/D = 3$ and 4 obtained by the experiment are shifted upward compared with the other streamwise locations (see Fig. 6c). This suggests that the discrepancies in the peak position of the wall-normal velocity between the LES and experiment at $x/D = 3$ and 4 might be affected by the uncertainty in the experiment. In fact the agreement between the LES and experiment at $x/D = 5$ is found to be very good.

All velocity components at the cross-view plane $x/D = 3$ with the turbulent and laminar crossflows are compared with the experiment [3] in Fig. 9. The results obtained for the fine mesh are shown in the left half of each figure and experiment on the right half. The mean velocity distributions predicted by the LES with turbulent crossflow are in good agreement with the experiment in terms of the size, location and strength of the pair of counter-rotating vortices. The location of peak wall-normal velocity along the symmetry plane $z/D = 0$ obtained by the experiment is somewhat shifted upward

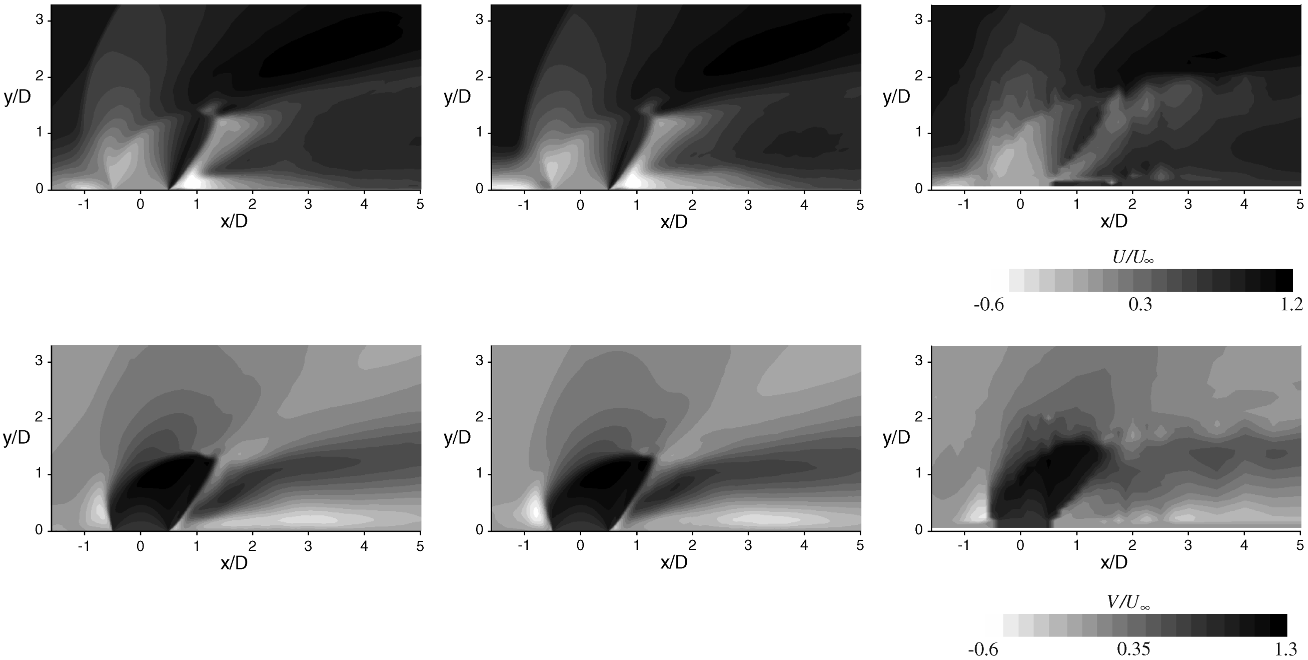

a) Turbulent crossflow **b) Laminar crossflow** **c) Experiment**

Fig. 6 Comparisons of mean streamwise (top) and wall-normal (bottom) velocity distributions between LES with turbulent and laminar crossflows on fine mesh and experiment [3] at midline plane $z/D = 0$. 20 equally spaced contours.

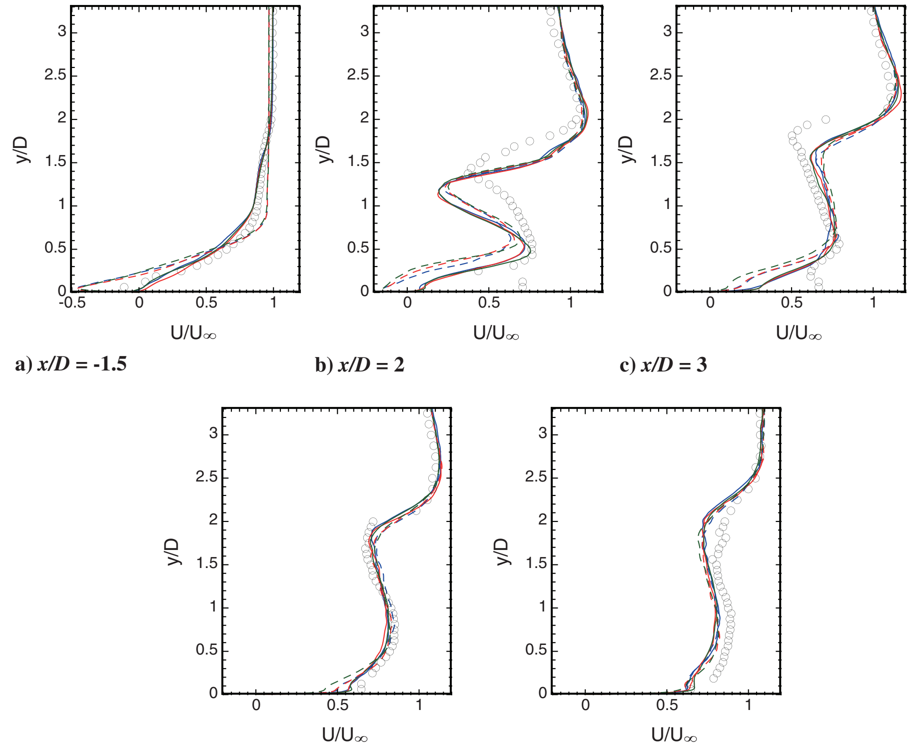

a) *x/D* = -1.5 b) *x/D* = 2 c) *x/D* = 3

d) *x/D* = 4 e) *x/D* = 5

Fig. 7 Comparisons of mean streamwise U/U_∞ velocity profiles between LES with turbulent and laminar crossflows on three levels of mesh resolution and experimental data [3] at $x/D = -1.5$, 2, 3, 4, and 5; solid lines: turbulent crossflow, dashed lines: laminar crossflow, blue line: fine mesh, red line: medium mesh, green line: coarse mesh, and ○: experiment.

compared with the LES. As discussed earlier, the experimental measurements of the wall-normal velocity at $x/D = 3$ and 4 are shifted upward (see Fig. 6c). Therefore the discrepancy in the peak position might be affected by the uncertainty in the experiment. The mushroom-shape structure in the streamwise velocity distributions obtained by the laminar crossflow case spreads out more laterally (i.e., in the spanwise direction) compared with the turbulent case and experiment. As discussed in Sec. III.B, two pairs of counter-rotating

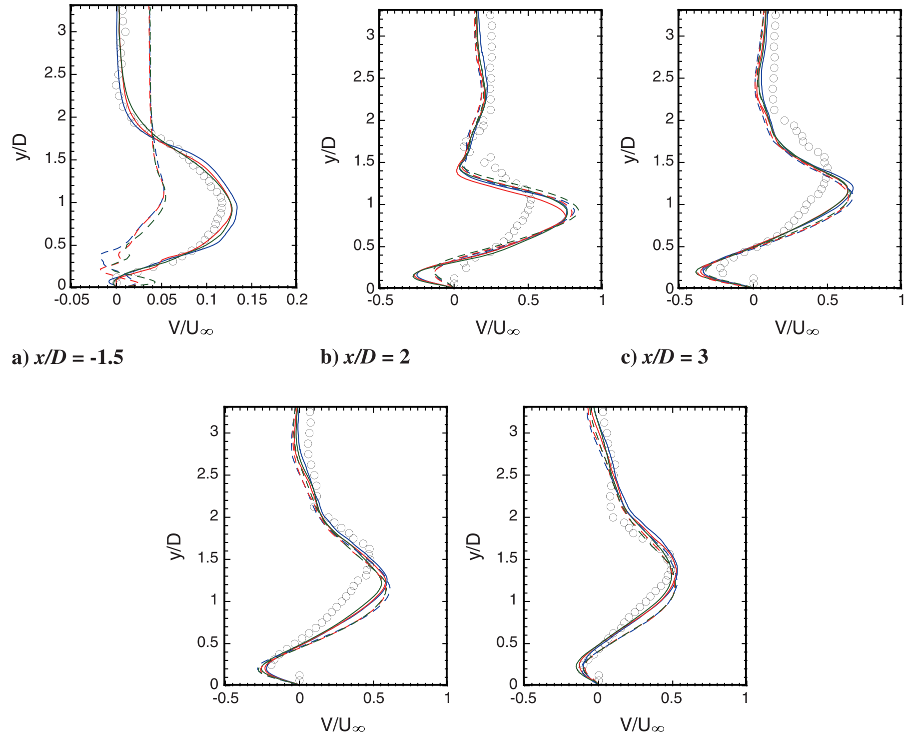

a) *x/D* = -1.5 b) *x/D* = 2 c) *x/D* = 3

d) *x/D* = 4 e) *x/D* = 5

Fig. 8 Comparisons of mean wall-normal V/U_∞ velocity profiles between LES with turbulent and laminar crossflows on three levels of mesh resolution and experimental data [3] at $x/D = -1.5$, 2, 3, 4, and 5; solid lines: turbulent crossflow, dashed lines: laminar crossflow, blue line: fine mesh, red line: medium mesh, green line: coarse mesh, and ○: experiment.

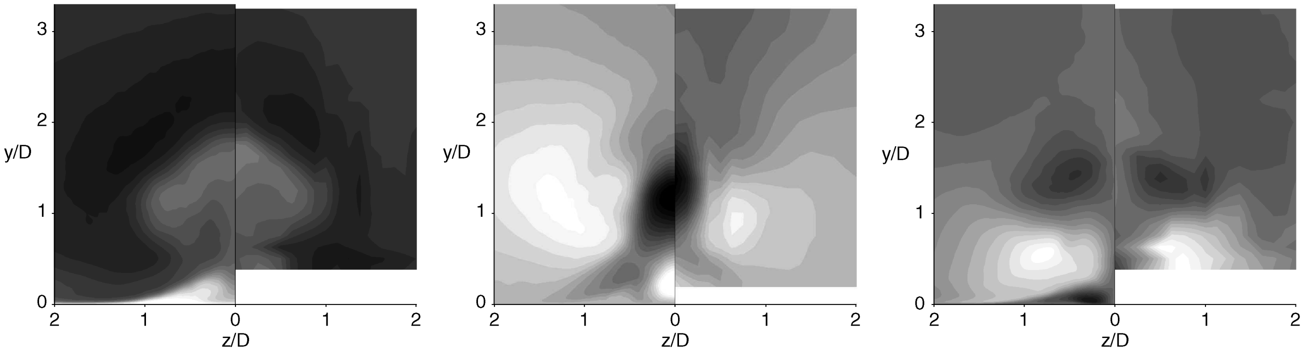

a) Turbulent crossflow

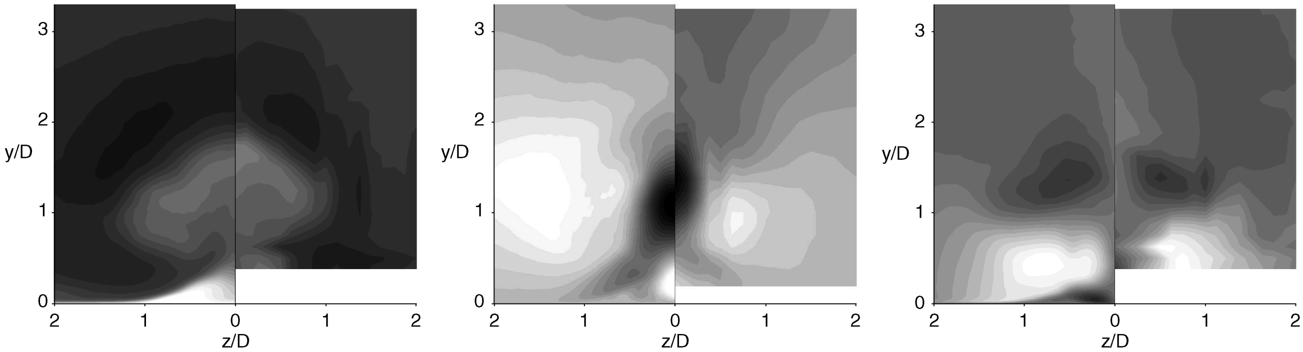

b) Laminar crossflow

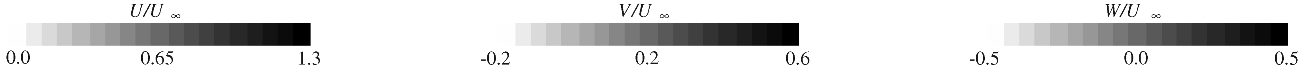

Fig. 9 Comparisons of mean streamwise (left), wall-normal (middle) and spanwise (right) velocity distributions between LES with turbulent and laminar crossflows on fine mesh and experiment [3] at cross-view plane $x/D = 3$. LES results on the left half of each figure and experiment on the right half; 20 equally spaced contours.

vortices are observed in Fig. 9. There is a strong upwash near the symmetry plane $z/D = 0$ downstream of the jet injection, due to the suction induced by the pair of counter-rotating jet vortices, which induces boundary-layer separation along the symmetry plane and scoops up and entrains the boundary-layer fluid into the jet vortices. The boundary-layer separation results in the other pair of counter-rotating vortices.

2. *Time-Averaged Wall Pressure*

Mean pressure distributions on the wall are compared in Fig. 10. The top half shows the experimental pressure-sensitive paint (PSP) measurement [4] and the bottom half shows the LES results with turbulent and laminar crossflows on the fine mesh. Figure 11 quantitatively compares the mean wall-pressure profiles obtained for the three levels of mesh resolution and the experimental data at three spanwise stations $z/D = 0$, 1, and 2. The mean wall-pressure distributions are grid converged. The LES with turbulent crossflow shows reasonable agreement with the experiment in terms of first pressure rise, due to the separation shock, relative low-pressure region downstream of the first peak, due to the horseshoe vortex, second pressure rise upstream of the jet injection induced by the bow shock and large low-pressure region in the jet downstream. The LES with laminar crossflow does not show the first pressure rise because of the absence of the upstream separation shock in the domain. Since the upstream separation region for the laminar case extends to the inlet boundary, as discussed earlier, the laminar case shows a weak separation shock generated from the inlet location $x/D = -5$. The upstream pressure mismatch is due to the weak separation shock. Downstream of the jet injection, the laminar crossflow case shows a

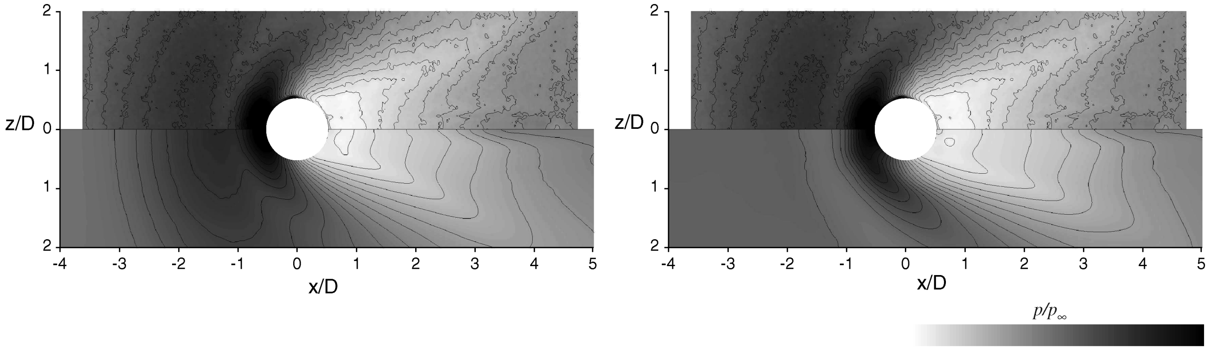

a) Turbulent crossflow

b) Laminar crossflow

Fig. 10 Comparisons of mean wall-pressure p/p_∞ distributions between LES (bottom half) with turbulent and laminar crossflows on fine mesh and experimental PSP measurement (top half) [4]; 20 equally spaced contour lines.

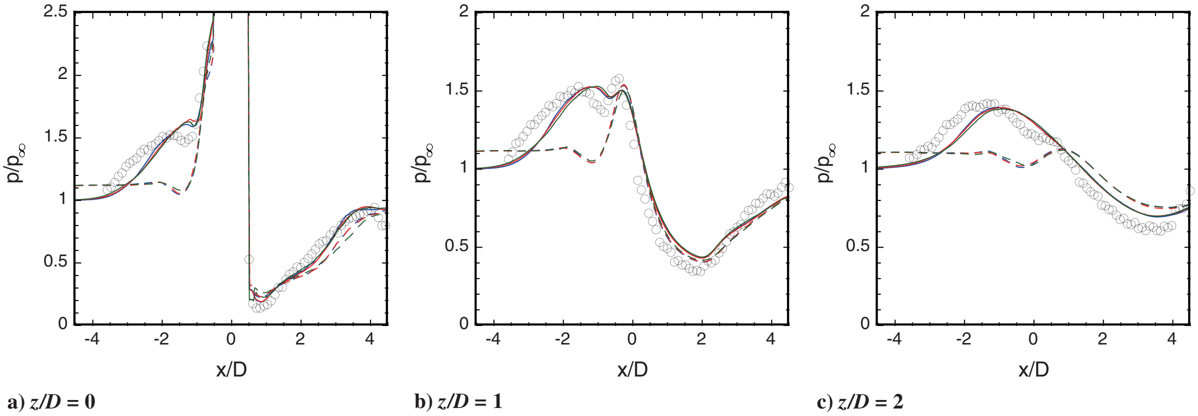

a) $z/D = 0$ b) $z/D = 1$ c) $z/D = 2$

Fig. 11 Comparisons of mean wall-pressure p/p_∞ distributions between LES with turbulent and laminar crossflows on three levels of mesh resolution and experimental PSP measurement [4] at $z/D = 0, 1,$ and 2; solid lines: turbulent crossflow, dashed lines: laminar crossflow, blue line: fine mesh; red line: medium mesh, green line: coarse mesh, and ○: experiment.

lower pressure along the symmetry plane $z/D = 0$ and a smaller spanwise extent of the low-pressure region compared with the turbulent case and the experiments.

3. Turbulent Statistics

Turbulent kinetic energy (TKE) distributions $(\langle u'u'\rangle + \langle v'v'\rangle + \langle w'w'\rangle)/2U_\infty^2$ and Reynolds shear stress $\langle u'v'\rangle/U_\infty^2$ at midplane $z/D = 0$ obtained by the LES with turbulent and laminar crossflows with the fine mesh are shown in Fig. 12. Figures 13 and 14 show the quantitative comparisons with the three levels of mesh resolution at downstream locations at $x/D = 0$, 1, 2, 3, and 4. Although the experimental data are available for the turbulent statistics, the experimental noise is much higher than for the mean quantities. Thus, we do not compare the LES results with the experimental data here. The results obtained by the fine and medium meshes show reasonable grid convergence in the turbulent statistics. Both the turbulent and laminar crossflow cases show three high-TKE regions and high negative Reynolds shear stress in the midline plane, corresponding to the windward and leeward sides of the jet boundaries and under the leeward jet boundary.

Comparing the turbulent statistics obtained by the fine mesh, the turbulent-crossflow case shows higher and more widely spread TKE and negative Reynolds stress in the windward jet boundary compared with the laminar case, whereas the leeward jet boundary shows a similar level of TKE and Reynolds stress. The higher and more widely spread TKE and negative Reynolds shear stress in the windward jet boundary suggest that the turbulent eddies in the crossflow excite the windward jet instability and enhances the subsequent jet mixing as will be discussed in Sec. III.E. It should also be noted that the laminar crossflow case shows higher TKE under the leeward jet boundary that extends to a larger region downstream compared with the turbulent case.

Figure 15 shows snapshots of density gradient magnitude at the midline plane $z/D = 0$ for the turbulent-crossflow case with three levels of mesh resolution. All three meshes show vortex formation along the windward and leeward jet boundaries. By refining the mesh, the finer flow features are resolved. The progressive mesh refinement allows for proper resolution of finer scale turbulent structures within the large-scale vortices, whereas the vortex structures are somewhat obscure in the coarse mesh. These fine structures within the large-scale vortices are also observed in the experimental

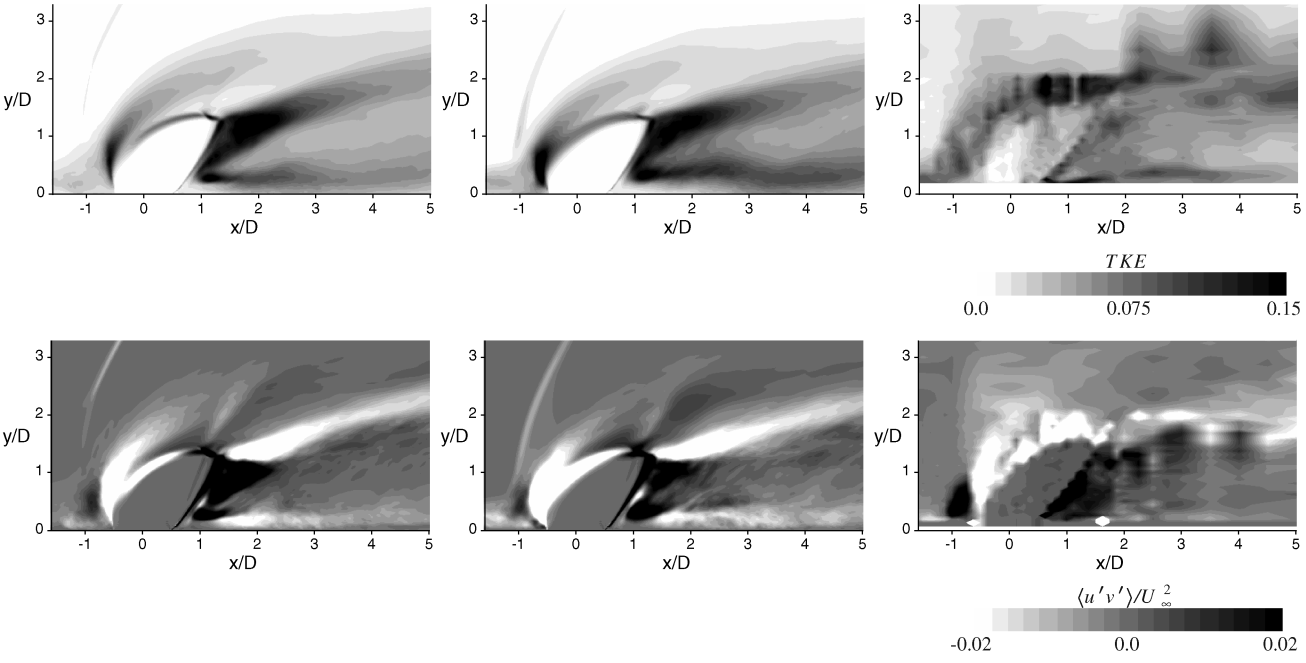

a) Turbulent crossflow b) Laminar crossflow c) Experiment

Fig. 12 Turbulent kinetic energy $(\langle u'u'\rangle + \langle v'v'\rangle + \langle w'w'\rangle)/2U_\infty^2$ (top) and Reynolds shear stress $\langle u'v'\rangle/U_\infty^2$ (bottom) distributions with turbulent and laminar crossflows on fine mesh and experiment [3] at midline plane $z/D = 0$; 20 equally spaced contours.

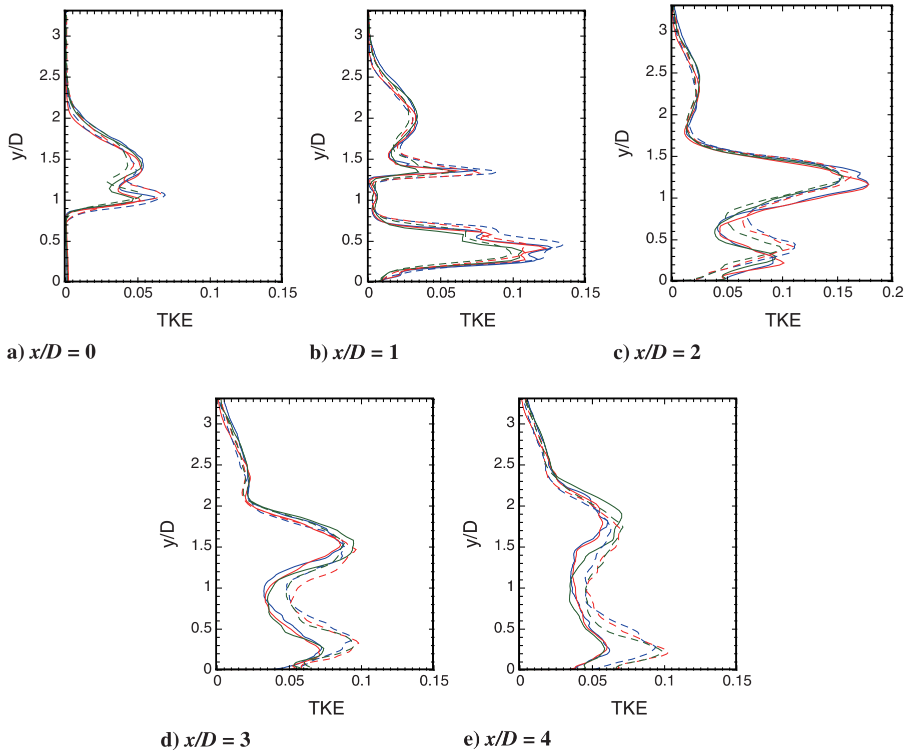

a) *x/D* = 0 b) *x/D* = 1 c) *x/D* = 2

d) *x/D* = 3 e) *x/D* = 4

Fig. 13 Turbulent kinetic energy $(\langle u'u'\rangle + \langle v'v'\rangle + \langle w'w'\rangle)/2U_\infty^2$ profiles at downstream locations $x/D = 0, 1, 2, 3,$ and 4 at midline plane; solid lines: turbulent crossflow, dashed lines: laminar crossflow, blue line: fine mesh, red line: medium mesh, and green line: coarse mesh.

schlieren images [1] (although the flow conditions are different). This is also evident in the Fourier spectra of spanwise velocity w/U_∞ at the windward ($x/D = 1.0$ and $y/D = 2.2$) and leeward ($x/D = 3.0$ and $y/D = 1.4$) jet boundary at the midline plane $z/D = 0$ in Fig. 16. Kolmogorov $-5/3$ law that shows inertial subrange is also included in the figure. The spectra yield insight into the range of scales of turbulence that are resolved in the simulations. As clearly shown, with increasing mesh resolution, a broader range of the inertial subrange is properly resolved in the LES.

Through the comparison between the LES with a series of progressive mesh refinements and available experimental data, we conclude that the statistics obtained by the present LES with turbulent crossflow show good agreement with the experiments, and the three levels of mesh refinement show reasonable grid convergence in the

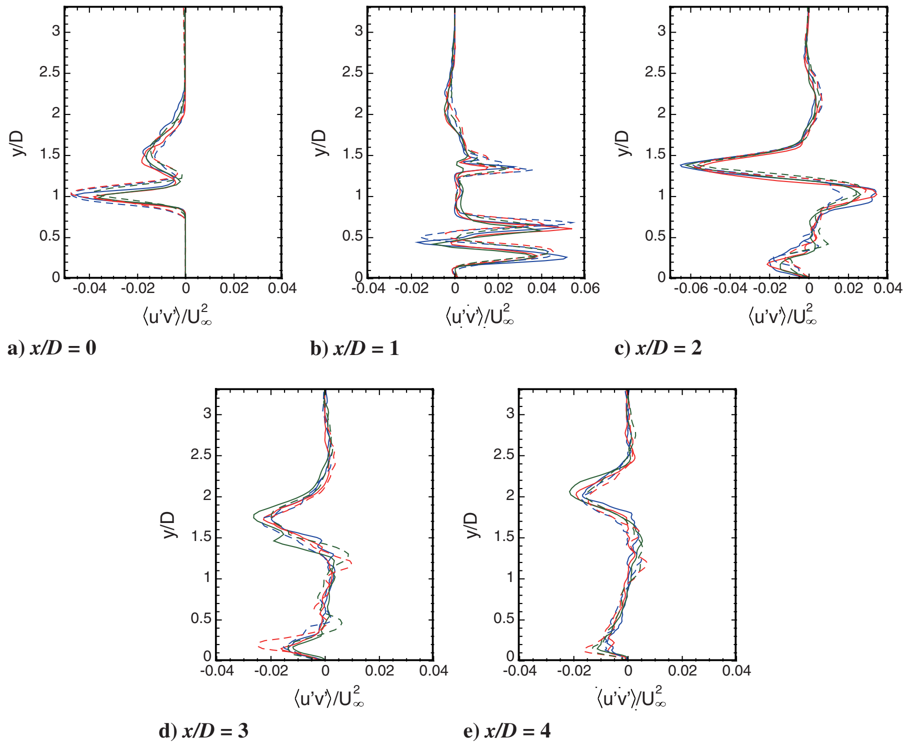

a) *x/D* = 0 b) *x/D* = 1 c) *x/D* = 2

d) *x/D* = 3 e) *x/D* = 4

Fig. 14 Reynolds shear stress $\langle u'v'\rangle/U_\infty^2$ profiles at downstream locations $x/D = 0, 1, 2, 3,$ and 4 at midline plane; solid lines: turbulent crossflow, dashed lines: laminar crossflow, blue line: fine mesh, red line: medium mesh, and green line: coarse mesh.

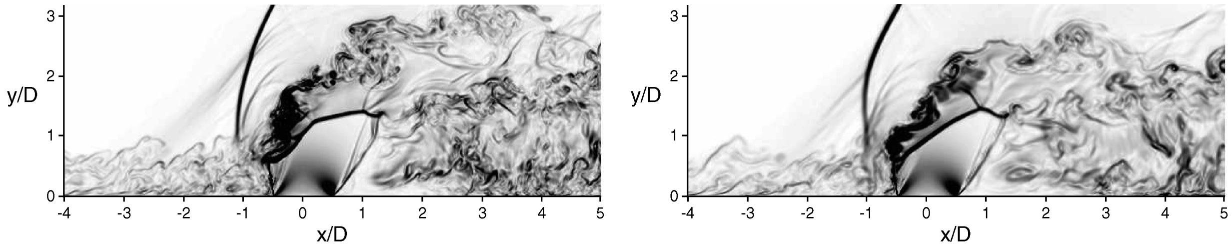

a) Fine mesh **b) Medium mesh**

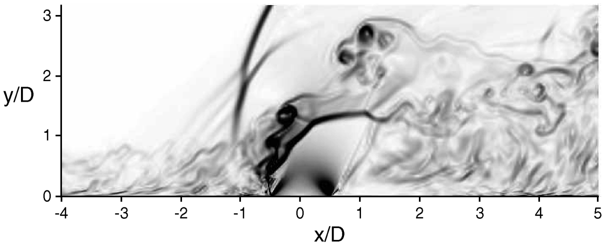

c) Coarse mesh

Fig. 15 Instantaneous snapshots of density gradient magnitude at midline plane $z/D = 0$ obtained by the three levels of mesh resolution with turbulent crossflow.

predicted mean and turbulent flow quantities. The progressive mesh refinement in combination with the high-resolution nondissipative numerical scheme allows for proper resolution of the turbulence. In the following, we therefore discuss the key physics of the jet mixing and the effect of turbulence in the upstream boundary layer on the mixing using the results obtained by the fine mesh.

D. Instantaneous Flowfields

1. *Two-Dimensional Slices of Flowfields*

Figure 17 shows instantaneous snapshots of density gradient magnitude and passive scalar of jet fluid obtained by the turbulent-crossflow case on the fine mesh. Side-, top-, and cross-view planes are obtained at $z/D = 0$, $y/D = 1$, and $x/D = 1$, 3, and 5. The high-order compact differencing scheme with localized artificial diffusivity methodology captures the 3-D unsteady front bow shock, upstream separation shock, barrel shock, Mach disk, acoustic waves, and contact surfaces without spurious wiggles and also simultaneously resolves a broad range of scales of turbulence. The turbulent eddies in the incoming boundary layer interact with the front bow shock and the windward jet.

Most of the jet fluid passes through the barrel shock and Mach disk; jet mixing progressively occurs after the jet fluid passes through the shocks. The vortex structures in the windward and leeward jet boundaries break down to finer well-developed turbulent eddy structures downstream. The turbulent structures play an important role in determining the behavior of jet fluid stirring and subsequent mixing, as clearly shown in the snapshots of the passive scalar. Because the jet fluid that passes through the barrel shock has larger velocity than the crossflow that passes through the bow shock, vortices developed along the windward jet boundary roll counterclockwise, as observed in the side view. The vortices also roll in the spanwise direction along the windward jet boundary as observed in the top view. Therefore, these vortices do not form a clear vortex ring but form 3-D complex vortex ringlike structures as will be discussed in Sec. III.D.2.

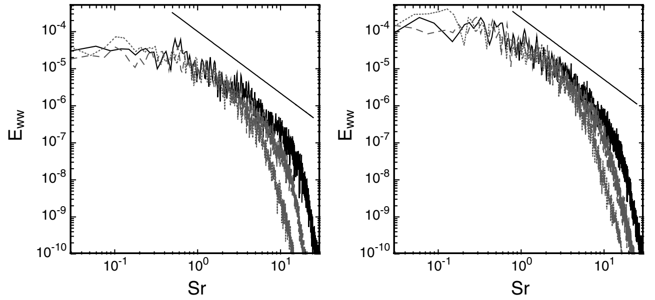

a) Windward jet boundary **b) Leeward jet boundary**

Fig. 16 Spectra of spanwise velocity w/U_∞ at windward ($x/D = 1.0$ and $y/D = 2.2$) and leeward ($x/D = 3.0$ and $y/D = 1.4$) jet boundaries at the midline plane $z/D = 0$ for turbulent-crossflow case with three levels of mesh resolution (including a line with $-5/3$ slope); black solid line: fine mesh, gray dashed line: medium mesh, and gray dotted line: coarse mesh; Strouhal number $Sr = f \times D/U_\infty$.

In addition to these vortices, additional vortex structures are observed under the leeward jet boundary in the side view. These vortices originate in the boundary-layer separation vortices and the vortices along the pair of the counter-rotating jet vortices (spanwise stirring), as shown in the cross views. The boundary-layer separation vortices exist along the symmetric plane downstream of the jet induced by the suction of the counter-rotating jet vortices. These turbulent structures create the high-TKE regions as observed under the leeward jet boundary in Fig. 5b.

On the leeward side of the jet, the side view of the jet fluid (Fig. 17b) shows thin filaments of jet fluid that are aligned normal to the jet trajectory. These filaments are observed close to the symmetry plane, where the pair of counter-rotating jet vortices induces upwash, the boundary layer separates, and the boundary-layer fluid is scooped up and entrained into the jet vortices. Su and Mungal [28] observe similar thin scalar filaments in their low-speed jet in crossflow experiments. They suggest that these filaments probably correspond to the wake vortices discussed by Fric and Roshko [29]. Figure 17d shows the jet fluid entrainment into the boundary-layer separation bubble along the symmetry plane downstream of the jet.

2. *Three-Dimensional Vortex and Jet Structures*

The 3-D features of vortex structures in side and top views are visualized by the instantaneous isosurfaces of the second invariant of velocity gradient tensor Q in Figs. 18a and 18c. The Q isosurfaces are colored by streamwise vorticity, which means that dark and light surfaces show clockwise and counterclockwise rotating vortices with the axis in the streamwise direction. The transparent gray-colored contour surface is the passive scalar of jet fluid distributions at the midline plane $z/D = 0$ in the side view and the wall-parallel plane $y/D = 1$ in the top view. Isosurfaces at $Y = 0.95$ of passive scalar of the jet fluid are shown in Fig. 18b to visualize the 3-D feature of the jet structures. Relatively fine vortex structures upstream of the jet injection show unsteady vortical motion inside the upstream

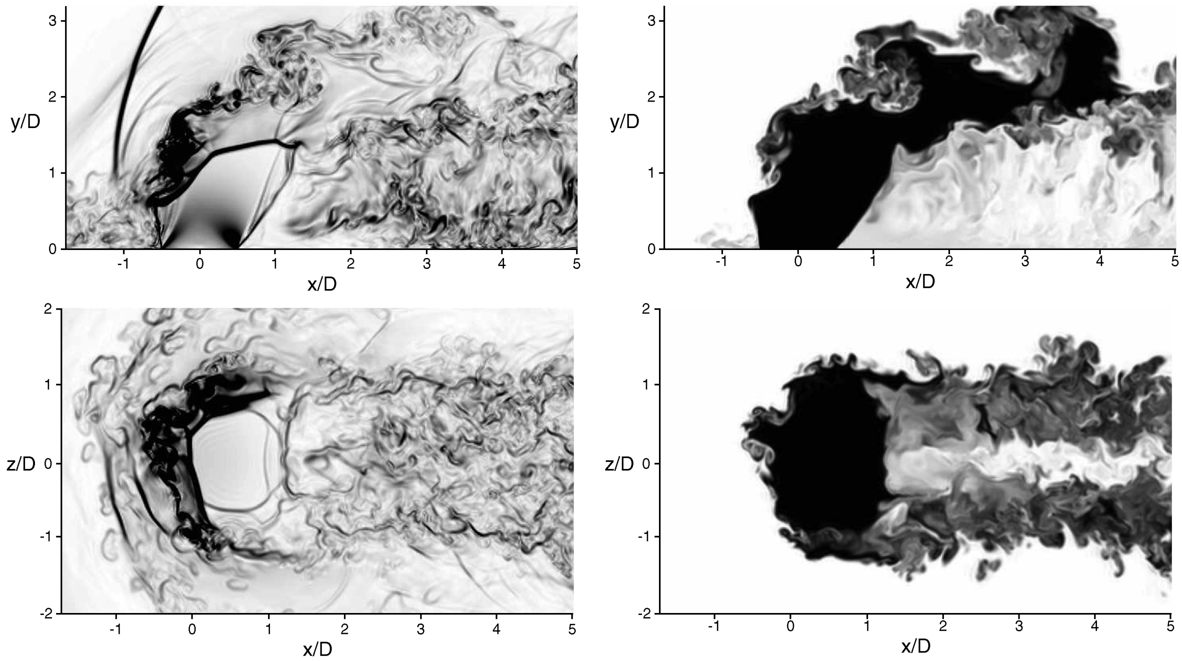

a) Density gradient magnitude: side and top views

b) Jet fluid (passive scalar): side and top views

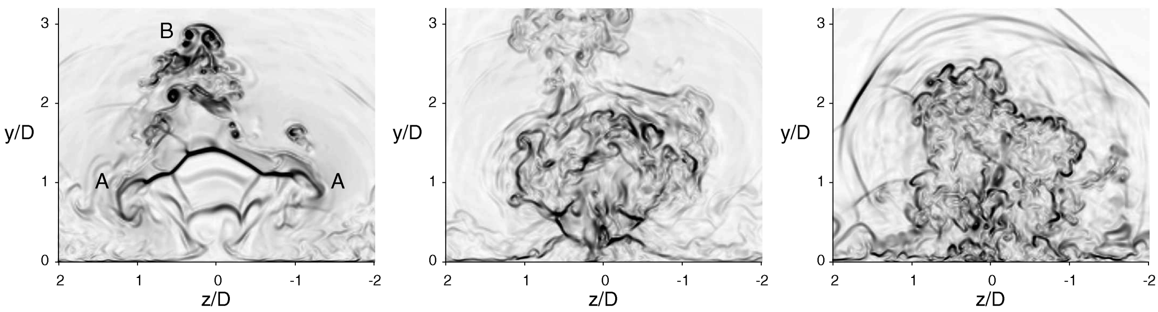

c) Density gradient magnitude: cross views at *x/D* = 1, 3 and 5

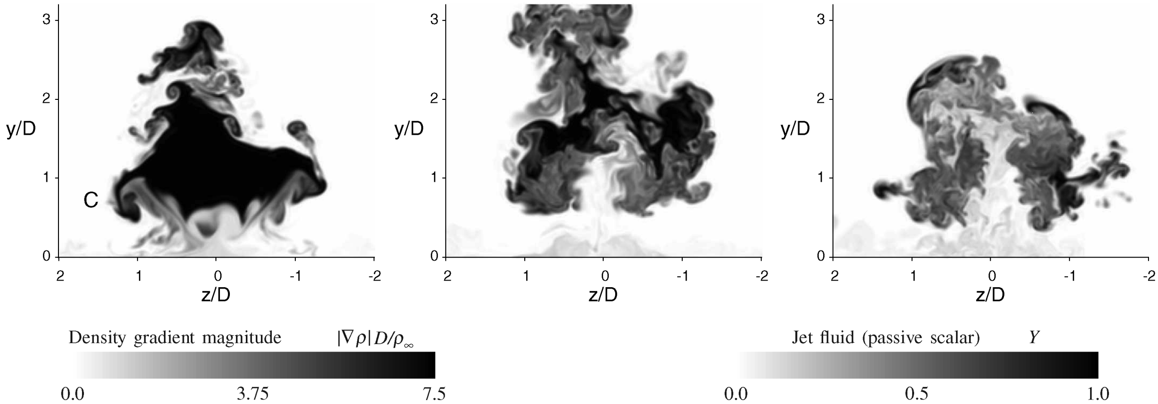

d) Jet fluid (passive scalar): cross views at *x/D* = 1, 3 and 5

Fig. 17 Instantaneous snapshots of density gradient magnitude and passive scalar of jet fluid at midline plane $z/D = 0$ (top), wall-parallel plane $y/D = 1$ (middle) and cross-view planes $x/D = 1$, 3, and 5 (bottom two, from left to right) obtained by the turbulent-crossflow case on fine mesh.

recirculation region, which form a horseshoe vortex in the time-averaged flowfields.

Clockwise and counterclockwise rotating strong longitudinal vortices are clearly observed by dark and light colored surfaces in the top view. Dark colored clockwise rotating longitudinal vortices are observed mainly in the lower half of the top view and the counterclockwise vortices are in the upper half. These longitudinal vortices form two groups of counter-rotating vortices, as shown in Figs. 18a and 18c. One group is a U-shaped pair of counter-rotating vortices that develop sideways from the symmetry plane with an upward inclination, as shown by location A in Figs. 18a and 18c (also in Fig. 17c at the $x/D = 1$ plane), which forms the pair of counter-rotating jet vortices in the mean flowfield, as shown in the cross view of Fig. 5a. The other group is the pair of counter-rotating vortices above the U-shaped vortices observed around the symmetry plane (B in Figs. 18a and 18c, and also in Fig. 17c at the $x/D = 1$ plane), which is called the upper trailing vortex in [6].

Along the longitudinal vortices, relatively small-scale hairpinlike vortices (gray-colored vortices) that do not have a vortex axis in the streamwise direction are generated further downstream. The

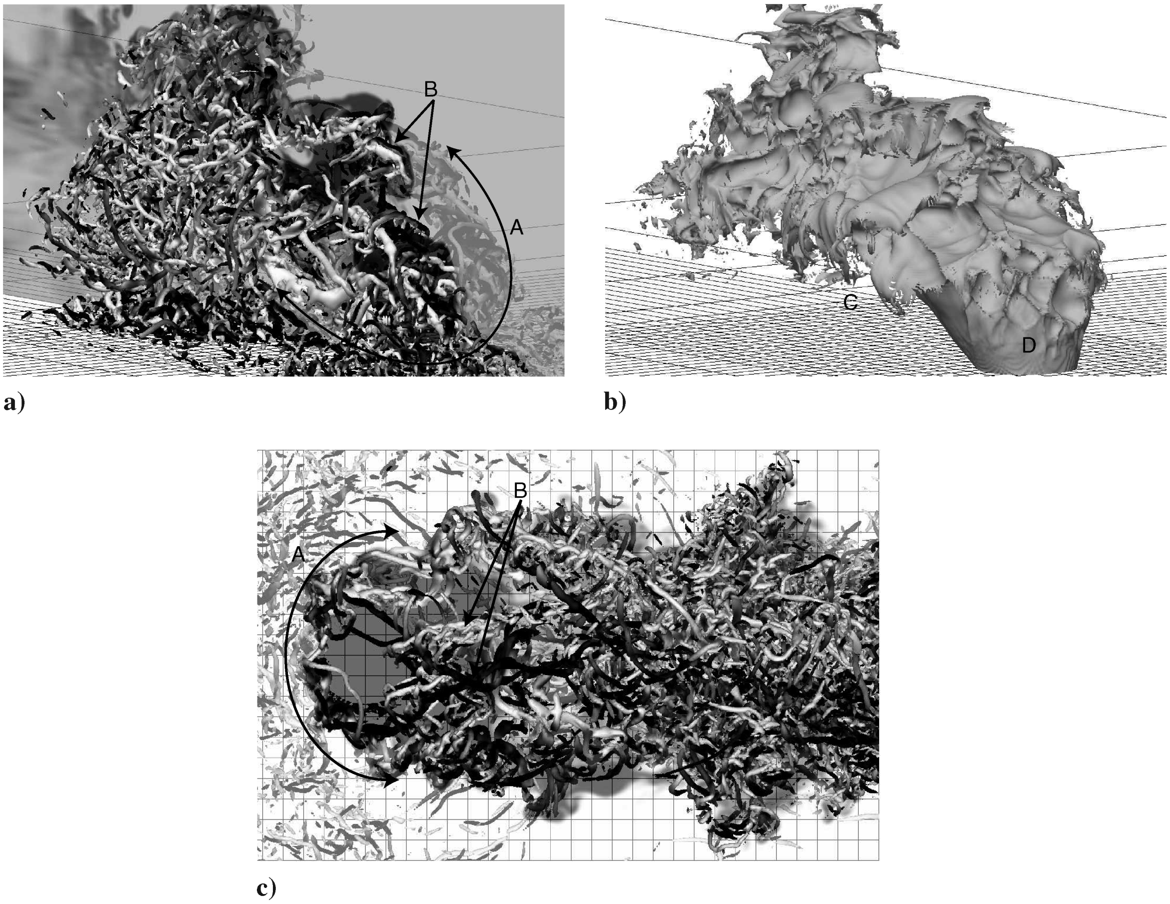

a)

b)

c)

Fig. 18 Instantaneous snapshots of vortex and jet structures obtained by the turbulent-crossflow case on fine mesh: a) side view of isosurfaces of the second invariant of velocity gradient tensor Q colored by streamwise vorticity with passive scalar of jet fluid distributions in transparent gray-colored contour surface at midline plane $z/D = 0$, b) top view of Q isosurfaces colored by streamwise vorticity with transparent gray-colored passive scalar contour surface at wall-parallel plane $y/D = 1$, and c) side view of isosurfaces of passive scalar of jet fluid at $Y = 0.95$.

relatively large-scale longitudinal vortex structures break down to finer and more random well-developed turbulent structures downstream approximately at $x/D = 2 \sim 3$. The isolated regions of vortex structures and resultant high TKE observed under the leeward jet boundary in the side view (Figs. 5b and 17) are due to these fine vortex structures along the jet boundary and the boundary-layer separation vortices along the symmetry plane induced by the suction of the U-shaped jet vortices.

Looking at the instantaneous jet structures shown in Fig. 18b, the jet surface is elongated along the relatively large-scale U-shaped longitudinal vortex structures (an example is observed at location C, also visible in Fig. 17d at the $x/D = 1$ plane). In the developed turbulent region, the jet surface also breaks down to finer and random structures, indicating the importance of these eddy structures that determine the behavior of jet fluid stirring and subsequent mixing. Interestingly, the windward jet surface at location D shows fish-scale-like structures. The structures are more complex than roller structures associated with quasi-ring-like vortices. This complex pattern is perhaps an effect of the impinging turbulent-boundary-layer structures.

3. *Large-Scale Dynamics of Shocks and Jet*

The simulated unsteady flowfield shows noticeable large-scale dynamics in the deformation of shock structures and associated vortex formation that entrains the crossflow and enhances the subsequent windward jet mixing. Time-history pressure data inside the upstream recirculation region and representative time-series snapshots of the passive scalar of jet fluid overlapped with negative dilatation contours at the midline plane are shown in Fig. 19 to illustrate these related dynamics. The negative dilatation contours highlight the compression in the flow such as shock structures and acoustic waves. The pressure-history data are obtained at location A in Fig. 19b. These 12 snapshots (Figs. 19b–19m) are taken at the time corresponding to the markers in the pressure history. The simulated unsteady flowfield illustrates that the pressure fluctuation inside the recirculation region upstream of the jet is coupled with the large-scale dynamics of the deforming barrel shock and bow shock and the accompanying large-scale vortex formation from the windward jet boundary. During the large-scale dynamics the barrel shock shows a kink in the time-series images.

Corresponding to the pressure rise from Fig. 19b to Fig. 19e in the pressure history, the degree of expansion at the windward side of the nozzle edge reduces to keep the pressure balance across the jet boundary. Because of the less expansion (lower Mach number distribution along the jet boundary) at Fig. 19c to Fig. 19e , the jet shear layer is able to support rapid growth of instability waves and starts to fluctuate. By way of contrast, the jet shear layer at Fig. 19b does not show such fluctuations.

Once the jet shear layer starts to fluctuate, a local shock wave appears within the jet because of the blockage of the supersonic jet by the deflected shear layer. Then, the local shock grows and connects to the original barrel shock, creating a kink in the barrel shock, as shown in Fig. 19e. In this time window, a second local shock wave appears and connects to the first local shock wave, showing the double kink in the barrel shock at Fig. 19f. The double kink in the barrel shock is not always present, and the following time window shows a single kink in the barrel shock, as shown in Fig. 19k. Once the kink appears, it moves downstream with an accompanying large-scale vortex and the jet shear layer rapidly deflects along the shock. The three shocks interact at the kink, making the triple point. The large-scale vortex entrains the crossflow, which stirs the jet fluid and enhances subsequent jet mixing. During the large-scale dynamics, an acoustic

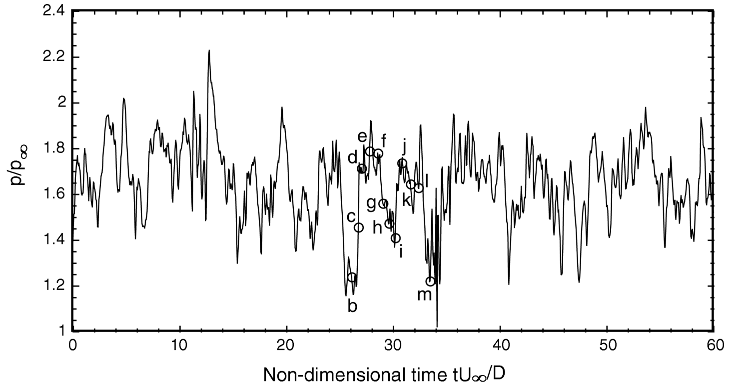

a) Time-history of pressure data inside upstream recirculation region

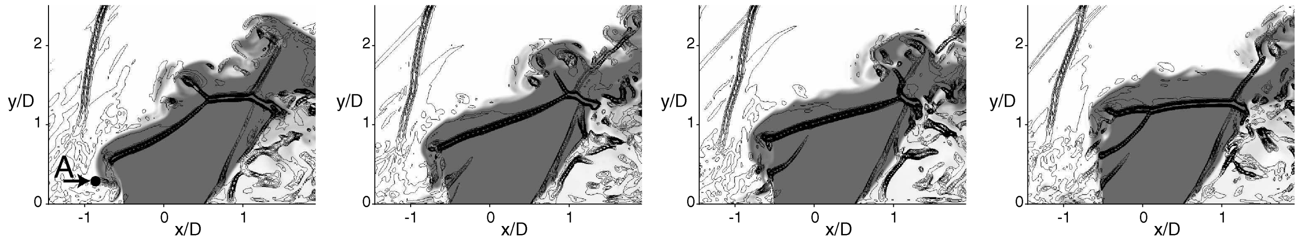

b) t=26.11 **c) t=26.74** **d) t=27.02** **e) t=27.79**

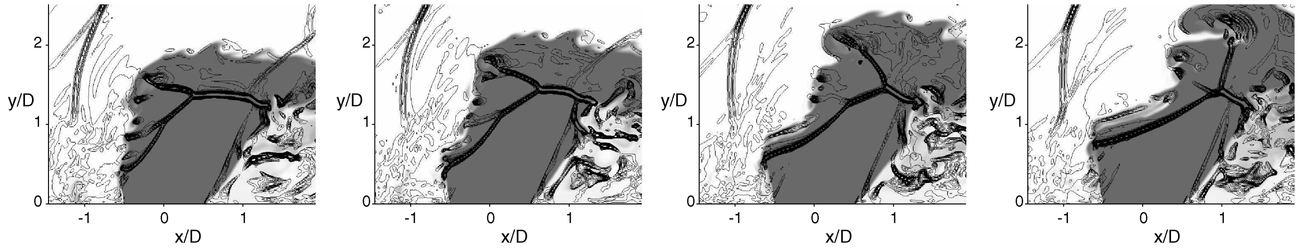

f) t=28.56 **g) t=29.04** **h) t=29.62** **i) t=30.19**

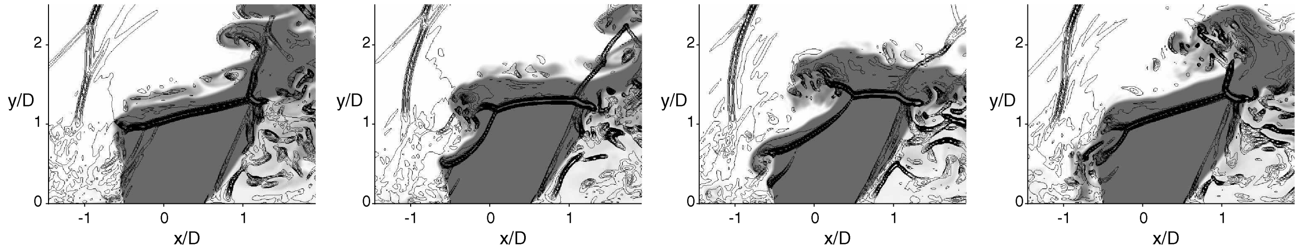

j) t=30.82 **k) t=31.63** **l) t=32.35** **m) t=33.46**

Fig. 19 Time-history pressure data inside the upstream recirculation region and representative time-series snapshots of jet fluid (passive scalar Y) overlapped with negative dilatation contours at midline plane $z/D = 0$ obtained by the turbulent-crossflow case on fine mesh. Nondimensional time, $t = t \times U_\infty/D$.

wave is generated and propagates upstream; it interacts with the bow shock (an example is observed in Figs. 19i and 19j). This interaction causes large-scale unsteady oscillation of the bow shock. Similar dynamics occur following this large-scale dynamics, as shown in Figs. 19j–19m. Similar large-scale dynamics (deformation of the shock structures and accompanying large-scale vortex) are also observed in the experiment [5], as shown in Fig. 20. Ben-Yakar et al. [1] also show similar front bow shock deformation and vortex formation in their consecutive schlieren images, although the flow conditions are different from the present LES.

Figure 21 shows the spectra of spanwise velocity at the mean windward jet boundary in the midline plane ($x/D = 1.0$, $y/D = 2.2$,

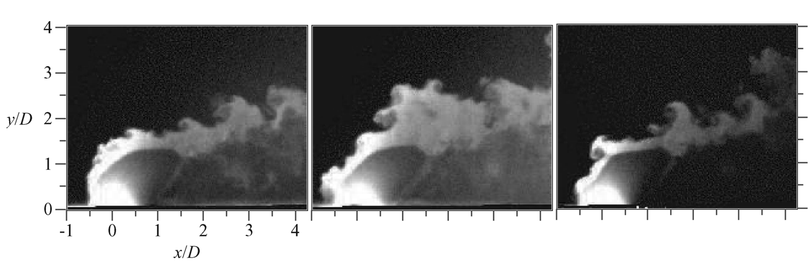

Fig. 20 Representative instantaneous experimental PLIF images at midline plane $z/D = 0$ (from VanLerberghe et al. [5]).

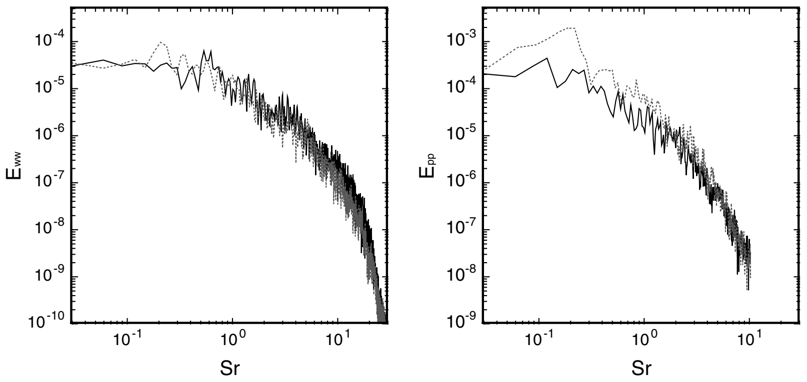

a) b)

Fig. 21 Spectra of a) spanwise velocity at the mean windward jet boundary and b) pressure at the upstream recirculation region; black solid line: turbulent crossflow with fine mesh, gray dotted line: laminar crossflow with fine mesh; Strouhal number $Sr = f \times D/U_\infty$.

and $z/D = 0$) and pressure inside the upstream recirculation region (location A in Fig. 19b) obtained by the turbulent and laminar crossflow conditions on the fine mesh. The peak in the spanwise velocity spectra indicate the frequency of the accompanying large-scale vortex formation. Although we discussed the dynamics by showing the turbulent-crossflow case, similar dynamics are also observed by the laminar crossflow case. The processes of the large-scale dynamics have a discrete frequency at $Sr = f \times D/U_\infty =$ 0.5–0.6 for the turbulent case and $Sr = 0.2$ for the laminar case and are repeated numerous times during the LES time history. Both the spanwise velocity and pressure spectra show the peak at the same frequency, further illustrating the coupling between the pressure fluctuations inside the recirculation region and the dynamics of shocks and accompanying vortex formation. It should be noted that the laminar case shows a clear peak in the spectra at $Sr = 0.2$, whereas the turbulent case does not show such a clear distinct peak.

4. Jet Entrainment Along Upstream and Downstream Separation Regions

Once large-scale counterclockwise roll-up of the jet shear layer occurs immediately after the jet passing through the barrel shock, the jet fluid is entrained into a region upstream of the jet, as shown in Figs. 19b–19d and Figs. 19l and 19m. The upstream entrainment of

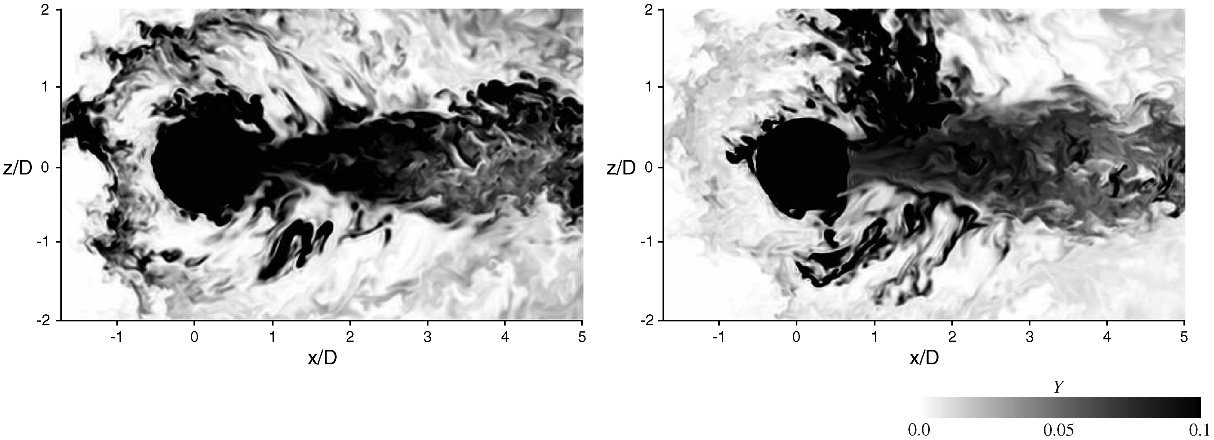

a) Jet fluid (passive scalar)

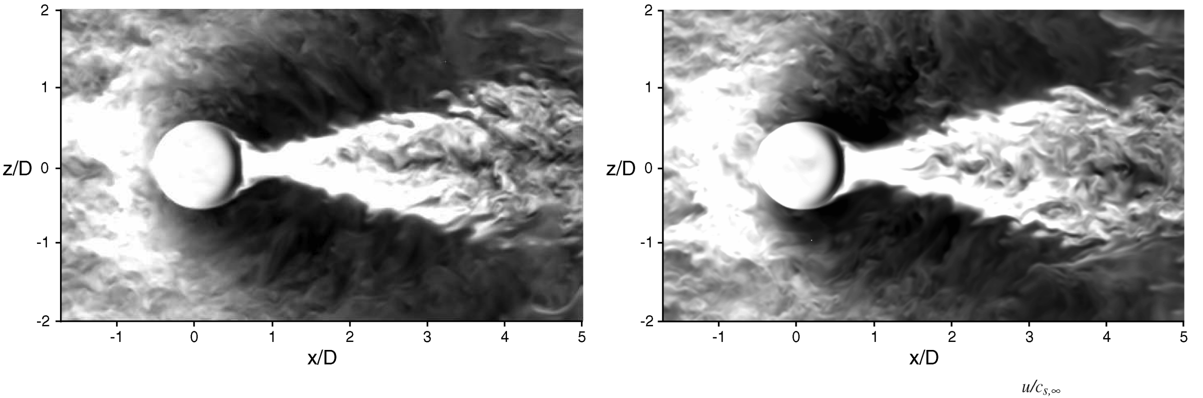

b) Streamwise velocity

Fig. 22 Representative instantaneous snapshots of passive scalar of jet fluid (top) and streamwise velocity (bottom) at wall-parallel plane close to the wall $y/D = 0.1$ obtained by the turbulent-crossflow case on fine mesh.

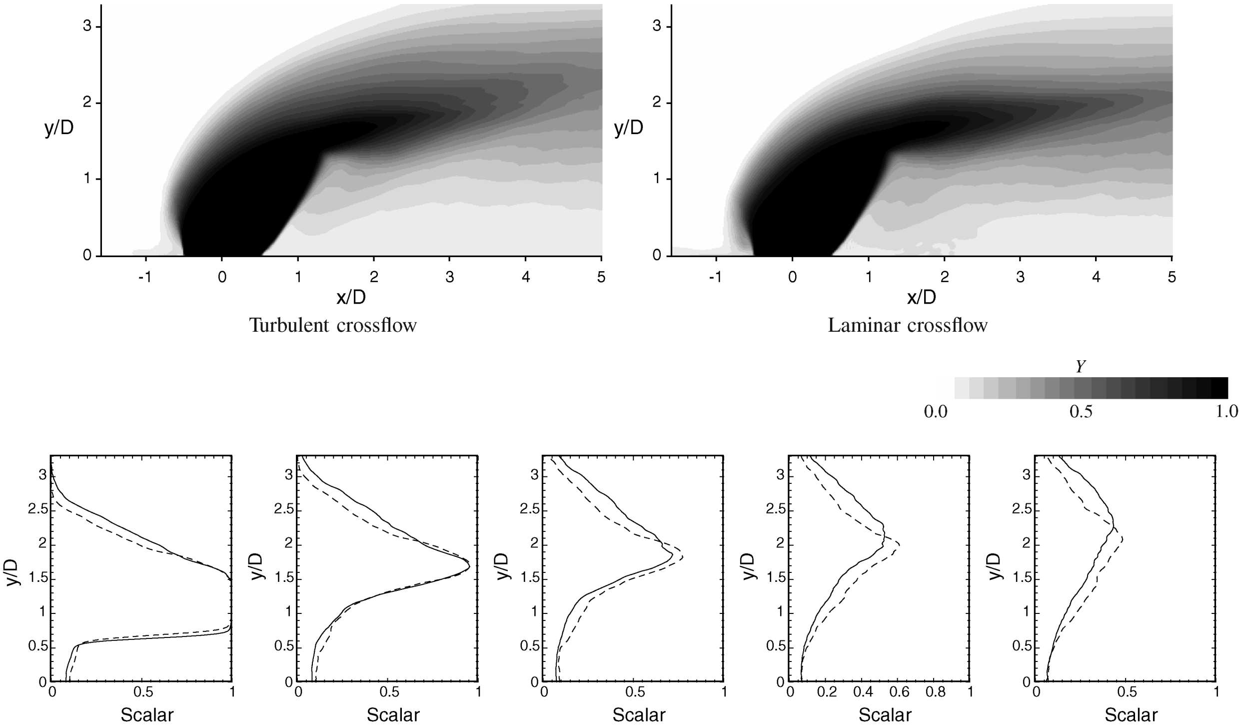

a) ***x/D*=1** **b)** ***x/D*=2** **c)** ***x/D*=3** **d)** ***x/D*=4** **e)** ***x/D*=5**

Fig. 23 Comparisons of mean passive scalar of jet fluid distributions between turbulent (top left) and laminar (top right) crossflow conditions on fine mesh at midline plane $z/D = 0$ and quantitative line plots (bottom) at downstream stations $x/D = 1, 2, 3, 4$, and 5; 20 equally spaced contour lines; solid line: turbulent crossflow and dashed line: laminar crossflow.

the jet fluid is also repeated in time associated with the large-scale dynamics of the shock waves and jet.

Figure 22 further illustrates the intermittent upstream jet mixing, also the continuous jet fluid entrainment into the boundary-layer separation bubble along the symmetric plane downstream of the jet. Two representative instantaneous snapshots of the jet fluid and streamwise velocity at a wall-parallel plane close to the wall ($y/D = 0.1$) are shown. Note that the passive scalar of jet fluid ranges from 0.0 to 0.1 in the figure. The plane intersects the instantaneous upstream and downstream boundary-layer separation regions (light colored regions in Fig. 22b) that form the horseshoe vortex and a pair of counter-rotating boundary-layer separation vortices along the symmetric plane, respectively, in the mean flow. The jet fluid entrainment is clearly observed along the upstream and downstream boundary-layer separation bubbles. The upstream jet fluid entrainment occurs intermittently associated with the repeated large-scale dynamics (the snapshot on the left clearly shows the upstream jet entrainment, whereas the right does not), although the jet mixing in the downstream separation bubble is continuous. These jet fluid entrainments may support the ignition of injected fuel along the separation regions upstream and downstream of the jet injection for a reactive species. Experimental OH-PLIF (planar laser-induced fluorescence of OH radicals) measurements by Ben-Yakar et al. [1] and Heltsley [30] show a strong OH-PLIF signal along these separation regions, although the flow conditions are different from the present LES. This indicates that the jet fluid mixing and resultant ignition occur along these upstream and downstream separation regions. The experimental result supports the mechanism of the jet fluid entrainment along the separation bubbles observed in the present LES.

E. Effect of Turbulent Crossflow on Mixing

To elucidate the effect of the approaching turbulent boundary layer on the jet mixing mechanisms, the results of the LES on the fine mesh with an incoming turbulent boundary layer is compared with that of

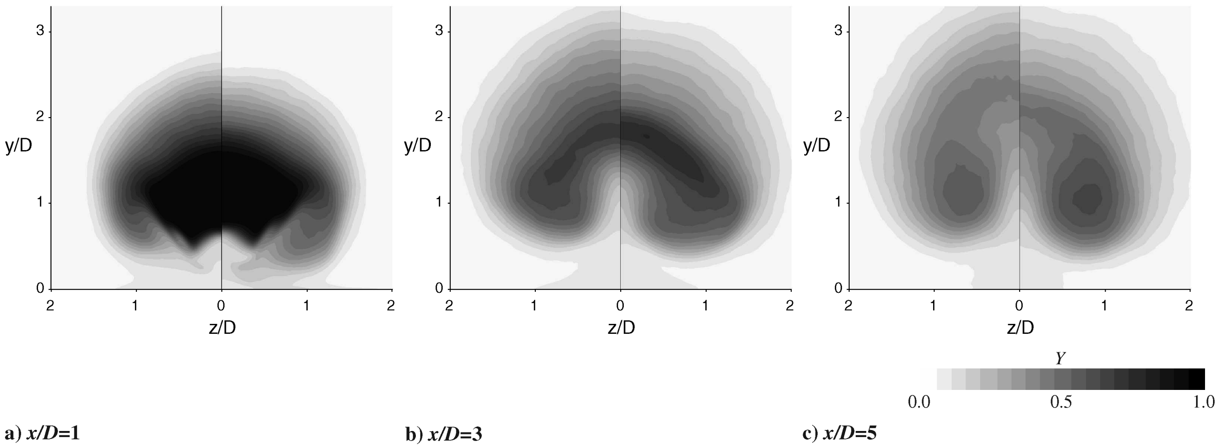

a) ***x/D*=1** **b)** ***x/D*=3** **c)** ***x/D*=5**

Fig. 24 Comparisons of mean passive scalar of jet fluid distributions between turbulent (left half) and laminar (right half) crossflow conditions on fine mesh at cross-view planes $x/D = 1, 3$, and 5.

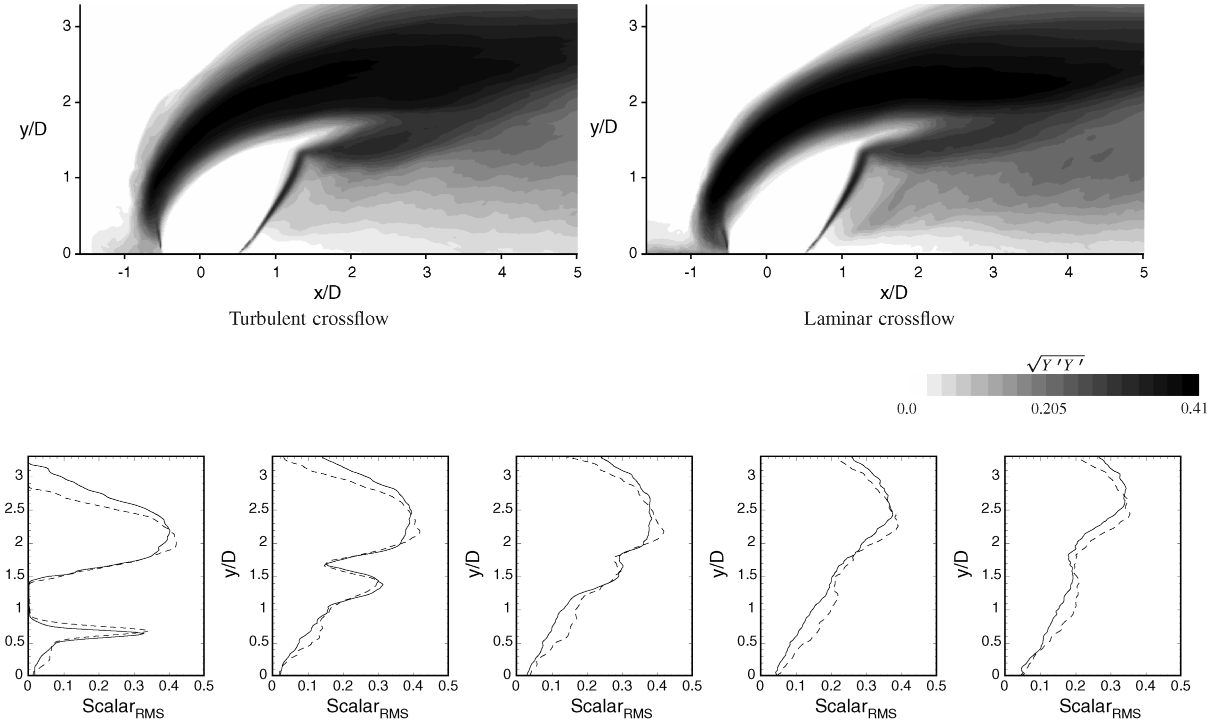

a) *x/D*=1 b) *x/D*=2 c) *x/D*=3 d) *x/D*=4 e) *x/D*=5

Fig. 25 Comparisons of rms of jet fluid tracer fluctuations between turbulent (top left) and laminar (top right) crossflow conditions on fine mesh at midline plane $z/D = 0$ and quantitative line plots (bottom) at downstream stations $x/D = 1, 2, 3, 4$, and 5; 20 equally spaced contour lines; solid line: turbulent crossflow and dashed line: laminar crossflow.

the laminar crossflow case by focusing on the passive scalar of jet fluid in this section.

Mean passive scalar (jet fluid) distributions at the midline plane $z/D = 0$ and quantitative comparisons at downstream stations $x/D = 1$, 2, 3, 4, and 5 obtained by the turbulent and laminar crossflow conditions on the fine mesh are shown in Fig. 23. Figure 24 compares the mean passive scalar distributions at cross-view planes $x/D = 1$, 3, and 5. The turbulent-crossflow case is shown in the left half and the laminar case is in the right half. As clearly shown, progressive mixing of the jet fluid along the windward jet boundary is observed by the turbulent-crossflow conditions compared with the laminar case. The turbulent-crossflow case shows progressive dilution of jet fluid in the windward jet boundary, resulting in the lower jet fluid concentration around the cores of the counter-rotating jet vortices at the jet downstream locations. In the downstream locations, the relatively small-scale hairpinlike vortices are observed, and large-scale longitudinal vortex structures break down to finer and random well-developed turbulent structures, as shown in Fig. 18. This indicates the importance of the turbulent structures that determine the behavior of jet fluid stirring and subsequent mixing.

These observations are supported when the rms of the jet fluid tracer fluctuations are compared in Figs. 25 and 26. The high-intensity region in the rms of jet fluid fluctuations obtained by the turbulent-crossflow case further spreads along the windward jet boundary compared with the laminar case, whereas the laminar case shows higher jet fluid fluctuations at the peak location. This large extent of the high rms of jet fluid in the windward jet boundary obtained by the turbulent-crossflow case indicates the progressive mixing of the jet fluid along the windward jet boundary as observed in Figs. 23 and 24.

Figure 27 shows a comparison between the turbulent and laminar supersonic crossflow conditions in the instantaneous snapshots of density gradient magnitude and passive scalar of jet fluid at the midline plane $z/D = 0$. Since the upstream separation region

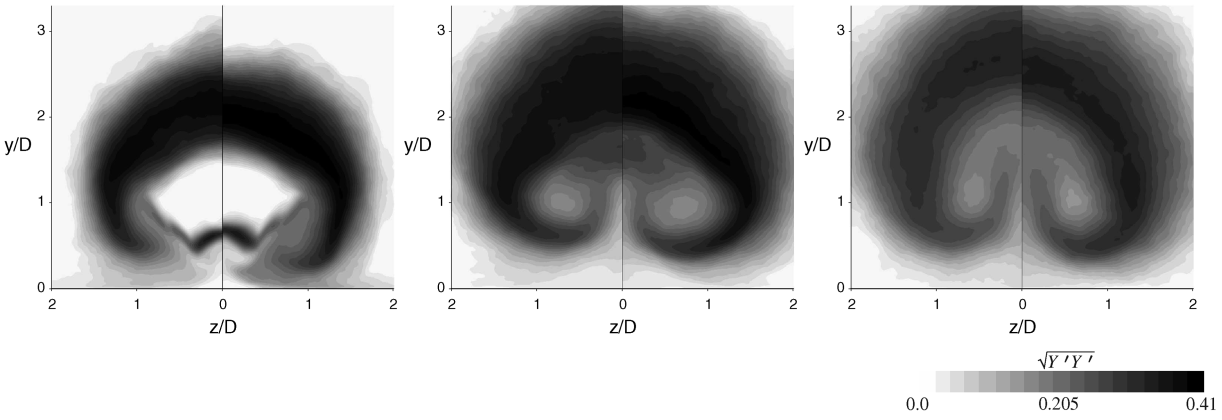

a) *x/D*=1 b) *x/D*=3 c) *x/D*=5

Fig. 26 Comparisons of rms of jet fluid tracer fluctuations between turbulent (left half) and laminar (right half) crossflow conditions on fine mesh at cross-view planes $x/D = 1$, 3, and 5.

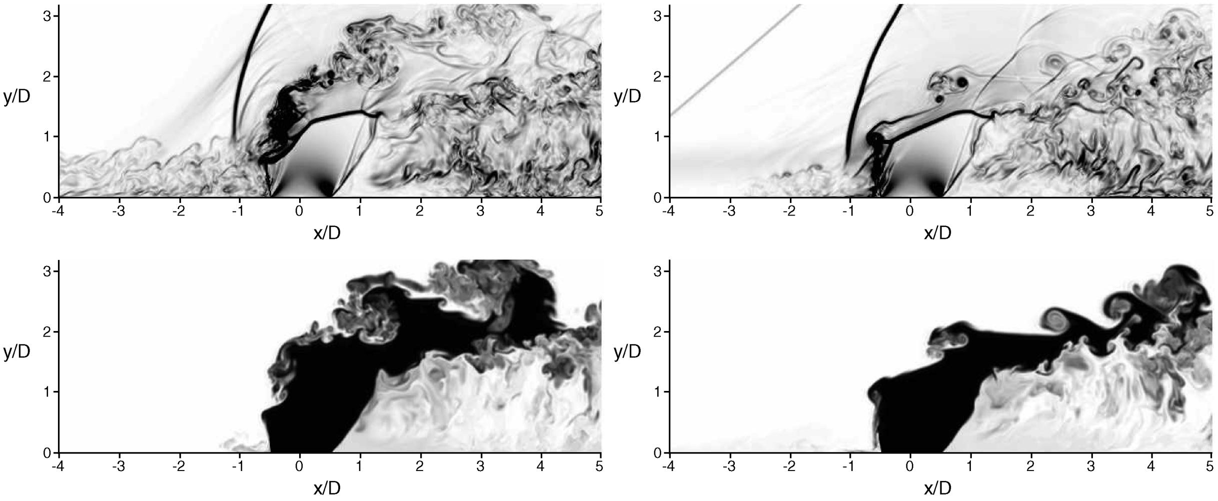

a) Turbulent crossflow **b) Laminar crossflow**

Fig. 27 Comparison of the instantaneous density gradient magnitude (top) and jet fluid (bottom) between turbulent and laminar crossflow conditions at midline plane $z/D = 0$ on fine mesh.

obtained by the laminar crossflow case extends all way up to the inlet boundary, as discussed in Sec. III.C, the laminar case shows a weak separation shock generated from the inlet location $x/D = -5$, whereas the turbulent-crossflow case shows the unsteady upstream separation shock appeared approximately from $-3 < x/D < -2$ location. In the turbulent-crossflow case, upstream turbulent structures interact with the bow shock and windward jet boundary. These interactions enhance the instability of the windward jet shear layer and support a more rapid breakdown in the jet shear layer structure to the turbulent state, whereas the laminar crossflow case shows the more laminarlike large vortex formation along the windward jet boundary. As a result, with the turbulent crossflow, the jet fluid is progressively stirred with the crossflow, entrained into the flow, and subsequently mixing is enhanced in the windward jet boundary, where high intensity of the jet fluid fluctuations and progressive jet dilution are observed. The evidence of more widely spread TKE and negative Reynolds stress distributions in the side view of the windward jet boundary shown in Figs. 12–14 also supports this observation. The higher peak in the jet fluid fluctuations observed by the laminar case shown in Fig. 25 is possibly due to the laminarlike vortices. The experimental observations [1] show that the ignition of injected fuel progressively occurs along the windward jet

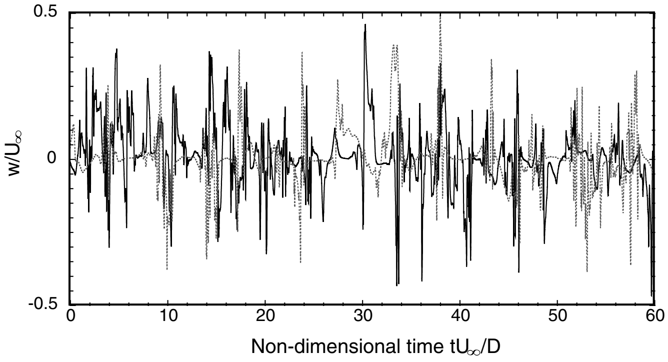

a) Time histories of spanwise velocity at *x/D*=1.0 and *y/D*=2.2

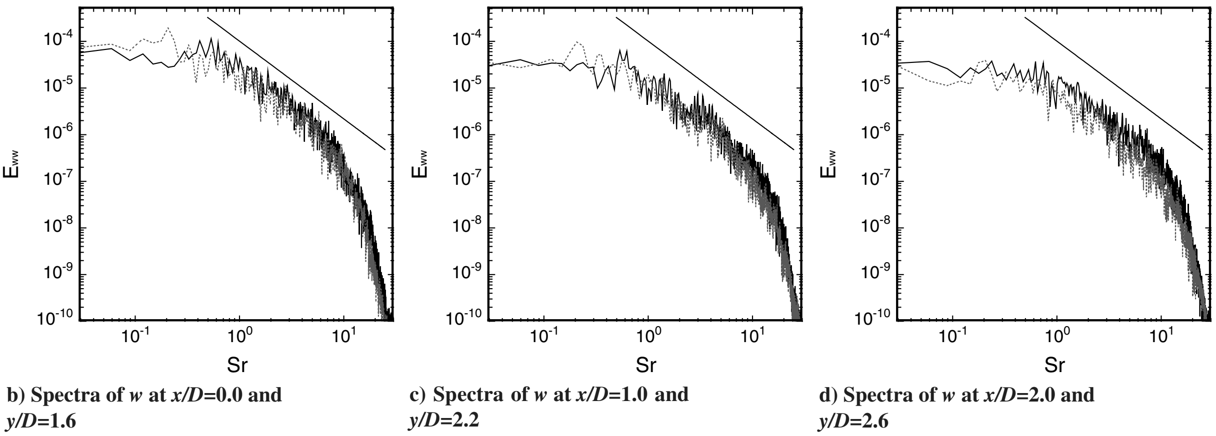

b) Spectra of *w* at *x/D*=0.0 and *y/D*=1.6 **c) Spectra of *w* at *x/D*=1.0 and *y/D*=2.2** **d) Spectra of *w* at *x/D*=2.0 and *y/D*=2.6**

Fig. 28 Time histories and spectra (with a line with $-5/3$ slope) of spanwise velocity along the mean windward jet shear layer on fine mesh at midline plane $z/D = 0$; black solid line: turbulent crossflow with fine mesh, and gray dotted line: laminar crossflow with fine mesh; nondimensional time $t = t \times U_\infty/D$ and Strouhal number $Sr = f \times D/U_\infty$.

boundary, thus illustrating the importance of the incoming turbulent-boundary-layer structures in predicting the mixing and resultant ignition.

Figure 28 further illustrates the excitation of the windward jet shear layer instability by the turbulent crossflow. Time histories of spanwise velocity w/U_∞ at $x/D = 1.0$ and $y/D = 2.2$ in the midline plane $z/D = 0$ and spectra of the spanwise velocity along the mean windward jet shear layer are shown in Fig. 28. Comparing the time histories of spanwise velocity and the time-series snapshots in Fig. 19, the spanwise velocity for the turbulent-crossflow case in Fig. 28a shows spikes when the large-scale vortices pass through the probe location approximately at $t = 26.11$, 30.19 and 33.46, as shown in Fig. 19 Thus, the spikes in the time histories of spanwise velocity indicate the passage of large-scale vortices at the probe point. The large-scale dynamics of shock deformation accompany vortex formation, as discussed in Sec. III.D. Consistent with the observations of the instantaneous flowfield in Fig. 27, the turbulent-crossflow case shows high-frequency fluctuations between the spikes, indicating the jet shear layer in the turbulent state. On the other hand, the laminar crossflow case shows the absence of fluctuations between the spikes, indicating the jet shear layer in the more laminarlike state. The spectra obtained by the turbulent crossflow show higher energy at the high frequency region along the windward jet trajectory. Interestingly, as discussed in section III.D, the frequency of the large-scale dynamics of shock deformation and accompanying vortex formation shows a higher frequency in the turbulent-crossflow case (Strouhal number $Sr = f \times D/U_\infty =$ 0.5–0.6) than the laminar crossflow case ($Sr = 0.2$), where the spectra show the peak. We note that the laminar case shows a clear peak at $Sr = 0.2$, whereas the turbulent case does not show such a clear peak.

IV. Conclusions

Large-eddy simulation (LES) of an underexpanded sonic jet injection into supersonic crossflows was conducted to obtain insight into the key physics of the jet mixing underlying the observed unsteady phenomena. A high-order compact differencing scheme with a recently developed localized artificial diffusivity scheme for discontinuity-capturing is used. The flow conditions are set based on the experiments of Santiago and Dutton [3], and detailed comparisons with these experimental data were shown. To keep the computational costs manageable, the calculations reported here do not match the Reynolds number of the experiment, but the boundary-layer thickness upstream of jet injection is matched. Jet mixing calculations in which the upstream boundary layer is fully turbulent were compared with corresponding calculations with a nominally laminar boundary layer to elucidate the effect of the approaching turbulent boundary layer on the jet mixing mechanisms.

Statistics obtained by the LES with turbulent crossflow showed good agreement with the available experiments. A progressive mesh refinement study is conducted to quantify the broadband range of scales of turbulence that are resolved in the simulations. The three levels of mesh refinement showed reasonable grid convergence in the predicted mean and turbulent flow quantities. Thus, the LES is suited for exploration of the physics and dynamics of the jet mixing in supersonic crossflows. The present LES also reproduces the large-scale dynamics of the flow and jet fluid entrainment into the boundary-layer separation regions upstream and downstream of the jet injection reported in previous experiments, but the richness of data provided by LES allows a much deeper exploration of the flow physics underlying the observed unsteady phenomena.

Key physics of the jet mixing in supersonic crossflows have been highlighted. Clockwise and counterclockwise rotating strong longitudinal vortices form two groups of counter-rotating vortices, a pair of U-shaped counter-rotating vortices that develop sideways from the symmetry plane with an upward inclination and a pair of counter-rotating vortices above the U-shaped vortices observed around the symmetry plane. Relatively small-scale hairpinlike vortices are generated along the longitudinal vortices. The relatively large-scale longitudinal vortex structures break down to finer and random well-developed turbulent structures downstream of the hairpin vortices. The jet surfaces are elongated along the relatively large-scale longitudinal vortex structures and break down to finer and random structures in the developed turbulent region, indicating the importance of these eddy structures that determine the behavior of jet fluid stirring and subsequent mixing. Interestingly the windward jet surface immediately after the nozzle exit shows fish-scale-like structures.

The simulated unsteady flowfield shows noticeable repeated large-scale dynamics of the deformation of shock structures and accompanying vortex formation. Pressure fluctuations inside the recirculation region are coupled with the large-scale unsteady dynamics of the barrel shock and the bow shock deformation and accompanying large-scale vortex formation in the windward jet boundary. During the repeated large-scale dynamics, rolled-up windward jet shear layer is entrained into a upstream separation region, showing the intermittent upstream jet fluid mixing. The simulated flowfield also show the continuous jet fluid entrainment into the boundary-layer separation bubble along the symmetry plane downstream of the jet injection.

Comparisons between the turbulent and laminar crossflow illustrate the importance of turbulent structures in the upstream boundary layer on the jet mixing mechanism. The interaction between the turbulent structures in the upstream incoming boundary layer and the jet enhances the instability of the windward jet shear layer, which supports a more rapid breakdown in the jet shear layer structure to the turbulent state. Thus, with the turbulent crossflow the jet fluid is progressively stirred with the crossflow, entrained into the flow, and mixing is subsequently enhanced.

Acknowledgments

This work is supported by the U.S. Air Force Office of Scientific Research (AFOSR) Multidisciplinary University Research Initiative (MURI) Program (grant FA9550-04-1-0387) with Julian Tishkoff as Program Manager. Computer time was provided by Japan Aerospace Exploration Agency (JAXA) Supercomputer System at JAXA and High Performance Computing Center at Stanford University. We gratefully acknowledge J. G. Santiago and J. C. Dutton for providing extensive experimental data and S. Pirozzoli for providing the direct numerical simulation data for the supersonic turbulent boundary. We are grateful to our AFOSR–MURI project collaborators, in particular, M. G. Mungal and W. N. Heltsley for various discussions on the upstream jet fluid mixing and E. Johnsen for comments on the manuscript. The present code is based on an extension to the code FDL3DI provided by M. R. Visbal, whom we thank.

References

[1] Ben-Yakar, A., Mungal, M. G., and Hanson, R. K., "Time Evolution and Mixing Characteristics of Hydrogen and Ethylene Transverse Jets in Supersonic Crossflows," *Physics of Fluids*, Vol. 18, No. 2, Feb. 2006, Paper 026101.
doi:10.1063/1.2139684

[2] Gruber, M. R., Nejad, A. S., Chen, T. H., and Dutton, J. C., "Mixing and Penetration Studies of Sonic Jets in a Mach 2 Freestream," *Journal of Propulsion and Power*, Vol. 11, No. 2, 1995, pp. 315–323.
doi:10.2514/3.51427

[3] Santiago, J. G., and Dutton, J. C., "Velocity Measurements of a Jet Injected into a Supersonic Crossflow," *Journal of Propulsion and Power*, Vol. 13, No. 2, 1997, pp. 264–273.
doi:10.2514/2.5158

[4] Everett, D. E., Woodmansee, M. A., Dutton, J. C., and Morris, M. J., "Wall Pressure Measurements for a Sonic Jet Injected Transversely Into a Supersonic Crossflow," *Journal of Propulsion and Power*, Vol. 14, No. 6, 1998, pp. 861–868.
doi:10.2514/2.5357

[5] VanLerberghe, W. M., Santiago, J. G., Dutton, J. C., and Lucht, R. P., "Mixing of a Sonic Transverse Jet Injected into a Supersonic Flow," *AIAA Journal*, Vol. 38, No. 3, March 2000, pp. 470–479.
doi:10.2514/2.984

[6] Viti, V., Neel, R., and Schetz, J. A., "Detailed Flow Physics of the Supersonic Jet Interaction Flow Field," *Physics of Fluids*, Vol. 21, No. 4, 2009, Paper 046101.

doi:10.1063/1.3112736

[7] von Lavante, E., Zeitz, D., and Kallenberg, M., "Numerical Simulation of Supersonic Airflow with Transverse Hydrogen Injection," *Journal of Propulsion and Power*, Vol. 17, No. 6, 2001, pp. 1319–1326. doi:10.2514/2.5881

[8] Peterson, D. M., Subbareddy, P. K., and Candler, G. V., "Assessment of Synthetic Inflow Generation for Simulating Injection into a Supersonic Crossflow," AIAA Paper 2006-8128, Nov. 2006.

[9] Jiang, G. S., and Shu, C. W., "Efficient Implementation of Weighted ENO Scheme," *Journal of Computational Physics*, Vol. 126, No. 1, 1996, pp. 202–228. doi:10.1006/jcph.1996.0130

[10] Larsson, J., Lele, S. K., and Moin, P., "Effect of Numerical Dissipation on the Predicted Spectra for Compressible Turbulence," *Annual Research Briefs 2007*, Center for Turbulence Research, Stanford, CA, 2007, pp. 47–57, http://www.stanford.edu/group/ctr/ResBriefs/ARB07.html [retrieved 2010].

[11] Johnsen, E., Larsson, J., Bhagatwala, A. V., Cabot, W. H., Moin, P., Rawat, P. S., et al., "Assessment of High-Resolution Methods for Numerical Simulations of Compressible Turbulence with Shock Waves," *Journal of Computational Physics*, Vol. 229, No. 4, Feb. 2010, pp. 1213–1237. doi:10.1016/j.jcp.2009.10.028

[12] Lele, S. K., "Compact Finite Difference Schemes with Spectral-like Resolution," *Journal of Computational Physics*, Vol. 103, No. 1, 1992, pp. 16–42. doi:10.1016/0021-9991(92)90324-R

[13] Kawai, S., Shankar, S. K., and Lele, S. K., "Assessment of Localized Artificial Diffusivity Scheme for Large-Eddy Simulation of Compressible Turbulent Flows," *Journal of Computational Physics*, Vol. 229, No. 5, March 2010, pp. 1739–1762. doi:10.1016/j.jcp.2009.11.005

[14] Cook, A. W., "Artificial Fluid Properties for Large-Eddy Simulation of Compressible Turbulent Mixing," *Physics of Fluids*, Vol. 19, No. 5, 2007, Paper 055103. doi:10.1063/1.2728937

[15] Kawai, S., and Lele, S. K., "Localized Artificial Diffusivity Scheme for Discontinuity Capturing on Curvilinear Meshes," *Journal of Computational Physics*, Vol. 227, No. 22, Nov. 2008, pp. 9498–9526. doi:10.1016/j.jcp.2008.06.034

[16] Mani, A., Larsson, J., and Moin, P., "Suitability of Artificial Bulk Viscosity for Large-Eddy Simulation of Turbulent Flows with Shocks," *Journal of Computational Physics*, Vol. 228, No. 19, October 2009, pp. 7368–7374. doi:10.1016/j.jcp.2009.06.040

[17] Cook, A. W., and Cabot, W. H., "A High-Wavenumber Viscosity for High-Resolution Numerical Method," *Journal of Computational Physics*, Vol. 195, No. 2, 2004, pp. 594–601. doi:10.1016/j.jcp.2003.10.012

[18] Gaitonde, D. V., and Visbal, M. R., "Padé-Type Higher-Order Boundary Filters for the Navier–Stokes Equations," *AIAA Journal*, Vol. 38, No. 11, Nov. 2000, pp. 2103–2112. doi:10.2514/2.872

[19] Obayashi, S., Fujii, K., and Gavali, S., "Navier-Stokes Simulation of Wind-Tunnel Flow Using LU-ADI Factorization Algorithm," NASA TM-100042, Feb. 1988.

[20] Iizuka, N., "Study of Mach Number Effect on the Dynamic Stability of a Blunt Re-Entry Capsule," Ph.D. Thesis, University of Tokyo, Tokyo, Feb. 2006.

[21] Beam, R. M., and Warming, R. F., "An Implicit Factored Scheme for the Compressible Navier–Stokes Equations," *AIAA Journal*, Vol. 16, No. 4, 1978, pp. 393–402. doi:10.2514/3.60901

[22] Yoon, S., and Jameson, A., "Lower-Upper Symmetric-Gauss–Seidel Method for the Euler and Navier–Stokes Equations," *AIAA Journal*, Vol. 26, No. 9, Sept. 1988, pp. 1025–1026. doi:10.2514/3.10007

[23] Urbin, G., and Knight, D., "Large-Eddy Simulation of a Supersonic Boundary Layer Using an Unstructured Grid," *AIAA Journal*, Vol. 39, No. 7, July 2001, pp. 1288–1295. doi:10.2514/2.1471

[24] Sherer, S. E., and Visbal, M. R., "Computational Study of Acoustic Scattering from Multiple Bodies Using a High-Order Overset Grid Approach," AIAA Paper 2003-3203, Jan. 2003.

[25] Van Driest, E. R., "Turbulent Boundary Layer in Compressible Fluids," *Journal of the Aeronautical Sciences*, Vol. 18, No. 3, March 1951, pp. 145–160.

[26] Pirozzoli, S., Bernardini, M., and Grasso, F., "Characterization of Coherent Vortical Structures in a Supersonic Turbulent Boundary Layer," *Journal of Fluid Mechanics*, Vol. 613, Oct. 2008, pp. 205–231. doi:10.1017/S0022112008003005

[27] Pirozzoli, S., Grasso, F., and Gatski, T. B., "Direct Numerical Simulation and Analysis of a Spatially Evolving Supersonic Turbulent Boundary Layer at $M = 2.25$," *Physics of Fluids*, Vol. 16, No. 3, March 2004, pp. 530–545. doi:10.1063/1.1637604

[28] Su, L. K., and Mungal, M. G., "Simultaneous Measurements of Scalar and Velocity Field Evolution in Turbulent Cross-flowing Jets," *Journal of Fluid Mechanics*, Vol. 513, 2004, pp. 1–45. doi:10.1017/S0022112004009401

[29] Fric, T. F., and Roshko, A., "Vortical Structure in the Wake of a Transverse Jet," *Journal of Fluid Mechanics*, Vol. 279, 1994, pp. 1–47. doi:10.1017/S0022112094003800

[30] Heltsley, W. N., "Structure and Stability of Reacting Jets in Supersonic Crossflow," Ph.D. Thesis, Stanford Univ., Stanford, CA, 2010.

P. Givi
Associate Editor